Thesis for the degree of licentiate of technology

Interaction between electronic and vibrational edge states in graphene

Anton Vikström

Department of Applied Physics
Chalmers University of Technology
Göteborg, Sweden 2015

Interaction between electronic and vibrational edge states in graphene
ANTON VIKSTRÖM

Department of Applied Physics
Chalmers University of Technology
SE–412 96 Göteborg
Sweden
Telephone +46–(0)31–772100

Cover: A schematic picture of a graphene sheet with an edge along the x-axis and an applied perpendicular magnetic field (purple). The electrons (red) follow localized Landau orbits in the bulk, but propagating "skipping orbits" near the edge. Along the edge there are also acoustic (Rayleigh) edge waves given by a 2D displacement field $\mathbf{u}$ (blue).

Typeset in LaTeX. Figures created using MATLAB and INKSCAPE.

Chalmers reproservice
Göteborg, Sweden 2015

Interaction between electronic and vibrational edge states in graphene
ANTON VIKSTRÖM
Department of Applied Physics
Chalmers University of Technology

ABSTRACT

A sheet of graphene in a magnetic field perpendicular to the sheet has electronic edge states with nonzero velocities. These edge states are localized to the edge of the sheet on the order of the magnetic length. In addition, there are also vibrational edge states —mechanical waves which propagate along the edge and decay exponentially into the bulk. These edge waves are analogous to the well-known surface acoustic waves in 3D systems; the edge being a 1D surface. This thesis considers a zigzag edge of a graphene sheet in a perpendicular magnetic field and investigates the interaction of in-plane vibrational edge waves with electronic edge states. It is found that propagation of low-amplitude vibrational edge waves is significantly blocked for certain acoustic wave vectors —those leading to resonant absorption due to electronic-acoustic interaction. For a finite gate voltage and a fixed acoustic frequency, tuning the magnetic field can bring the system through a number of such electronic resonances. Considering vibrational edge waves of larger amplitude, so that nonlinear effects become important, it is further demonstrated that the coupled system of electronic and acoustic equations has family of solutions in which the mechanical displacement is in the shape of a localized and stable profile traveling along the edge —a soliton. This type of acoustic soliton can attain velocities significantly higher than the speed of sound.

KEYWORDS: graphene, quantum Hall effect, edge waves, quantum acoustics, collective excitations, solitons.

LIST OF PUBLICATIONS

This thesis consists of an introductory text and the following papers:

I **Propagation of acoustic edge waves in graphene under quantum Hall effect**
A. Vikström
Low Temperature Physics **41**, pp. 381–388 (2015)

II **Hypersonic edge solitons in graphene under quantum Hall effect**
A. Vikström and L. Gorelik
Manuscript submitted to a scientific journal

Contents

Chapter 1

Introduction

1.1 Graphene

Carbon is an element that comes in many forms. In one form, it is diamond, the valued crystal famed for its hardness, in another form, it is graphite, the black substance in your pencil which rubs off on paper to form words, images and the casual doodle. Both diamond and graphite are entirely made up of carbon; no atoms of any other element are present[1]. The difference between them is that of *structure*. Both diamond and graphite are crystals, i.e. they are made up of a vast number of atoms bonded to each other in a repeating pattern, essentially forming one huge molecule. In diamond, the carbon atoms are bonded to each other in a complicated three-dimensional structure, but in graphite they form clearly separated and weakly connected layers of hexagonal grids [1]. The long and relatively weak bonds between these layers are what makes pencils work; when the pencil tip rubs against the paper[2], graphite layers are torn loose and end up affixed to the surface. In diamond, there are no such weakly connected layers, which is one of the reasons there are no diamond pencils. Different versions of the same element that differ only by their crystal structure are referred to as *allotropes* of that element, from Greek *allos* (“other”) and *tropos* (“form”).

There are many more allotropes of carbon than the two mentioned. In fact, a new allotrope has been discovered almost on a decennial basis during the last 30 or so years. Fullerenes, or “buckyballs”, are best described

---

[1] Or rather, if they *are* present, they are regarded as impurities.

[2] . . . or e.g., canvas, school desk, bathroom door.

as "carbon soccer balls" and became a popular field after their discovery in 1985 [2, 3]. A lecturer of mine once, somewhat jovially, described the zeitgeist as "Everyone dropped everything and started doing fullerenes". Not long after, the fullerene hype was largely superseded by the discovery[3] of carbon nanotubes in 1991 [5]. Carbon nanotubes are best described, both visually and mathematically, as a single graphite layer rolled up and connected into a cylindrical tube. Because of this simple relation to graphite layers, many results carried over from earlier theory. Graphite had long since been modeled theoretically by, at least as a first step, considering just a single layer, so a great deal was already known of single graphite layers [6, 7, 8]. To model a carbon nanotube as a rolled-up sheet simply meant taking the old theory and adding to the model that if you go far enough in one direction, you end up where you started, since you moved around the circumference of the tube [9]. Carbon nanotubes became a popular field and additions were made to the old graphite-layer theory; additions which, in the next paragraph, were modified to fit the rolled-up geometry of the nanotubes [10].

Then, in 2004, the now famous researchers and Nobel laureates A. Geim and K. Novoselov demonstrated the isolation of *individual* graphite layers [11]. Yet another carbon allotrope had been discovered: a crystal only *one atom* thick, the smallest thickness conceivable. While single graphite layers had been studied theoretically for ages, the actual existence of a stable 2D structure had always been considered infeasible [3, 12]. Moreover, the feat had been accomplished by an astonishingly simple technique now known as the "scotch-tape method". Basically, they started with a piece of graphite, put a piece of scotch tape on it, and tore it loose. The tape was now thinly coated with graphite. By again using tape to tear loose graphite from that, an even thinner graphite coating was obtained. By repeating this several times, they ended up with a piece of tape covered by an extremely thin coating of graphite. They were then able to confirm the presence of isolated, single-layer graphite, thus proving that what had been a useful theoretical construct for decades, was actually a practical reality [11]. Because of its earlier use in describing other allotropes, the theory of graphene predates its discovery, and thus gave the new material a running start. Graphene was born.

---

[3] Carbon nanotubes had actually been discovered already in 1952 [4], but since the findings were published exclusively in Russian, in a Soviet journal, they were doubly obscured from the global research community behind both a language barrier and an iron curtain.

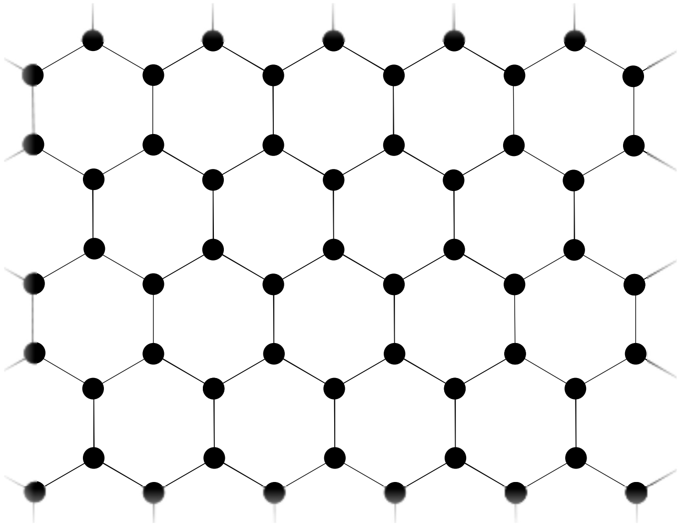

Figure 1.1: The "honeycomb" atomic lattice of graphene. Each black dot represents a carbon atom and the lines connecting them are atomic bonds. Graphite is made up of several such layers stacked on top of each other, connected by weak bonds.

As in the case of fullerenes and nanotubes, "everyone dropped everything and started doing graphene". This time, the hype was, perhaps, more warranted than ever. Graphene is a two-dimensional material in a three-dimensional world, so the electrons within are restricted to movement in a plane. However, graphene is also flexible; it can not just contract and expand, but can vibrate out of plane [13], so the electrons actually move in a a *contracting* and *curving* two-dimensional plane. And because of the way the carbon atoms are arranged, it turns out that the equations describing electrons in graphene are identical to those used to describe certain relativistic particles of zero mass [14]. The appeal of the material goes even further. Graphene is a superior conductor of electricity [11, 15], and despite being as thin as physically possible, it is incredibly strong [16]. Its strength has been illustrated by the cartoon picture of a cat sitting safely on a square-meter sheet of graphene supported only at the edges. The graphene would bend, but it would not break, and the mass of that graphene sheet would be roughly that of one of the whiskers of the cat [17]. The strength of graphene is due to the strength of the bonds between the carbon atoms and the hexagonal crystal structure. The hexagonal configuration of carbon atoms is actually the densest possible, since hexagonal tiling (Fig. 1.1) is the optimal way to partition a surface into equal geometrical shapes; this known as the honeycomb conjecture [18], so named because of its application by bees in honeycombs[4]. This dense structure also makes graphene highly impermeable to gasses and liquids [19]. In contrast, its negligible thickness makes it highly transparent to light [20], which is why researchers are currently using it in development of the next generation of touch screens [21].

Graphene is the thinnest [22], densest, strongest [16], most electrically conductive material in the world [11, 15], and a two-dimensional, flexible, transparent [20] membrane with remarkable electronic behavior to boot [13]. For this reason it has been nicknamed “the material of superlatives”. This thesis is an investigation into one particular phenomenon possible in this material, or to be specific, on the edges of graphene sheets. So, having taken a wide view of this growing field, I will now turn my eyes from the horizon, down to the desk, and focus on my recent contributions to it.

1.2 Brief Description of the Thesis

Before going into detail, I would now like to give a brief, simplified, and hopefully intuitive, description of the research presented in this thesis.

I consider a sheet of graphene suspended in a perpendicular magnetic field. Electrons in a magnetic field experience a force which is perpendicular to both their own motion and the field, the Lorentz force, which causes them to move in circular orbits whose radii decrease with magnetic field strength (since the force increases and makes them do sharper turns); this is also true for the electrons inside the graphene sheet. If we look at the behavior near an edge of the sheet, we can think of the electrons “bouncing” against the edge, causing them to “skip” along it (see cover). We call this image of electron behavior *skipping orbits* and note that the further we move the center of an electron orbit toward and outside the edge, the more tightly the orbits are squeezed against the edge, so the paths of the electrons become straighter, thereby increasing their effective velocity along the edge. This naïve picture does in fact capture many of the features of the system. A net flow of electrons consistutes a current, so we can conclude that there are

---

[4] Bees developed their engineering technique by a long, evolutionary process of trial and error, and never presented a rigorous mathematical proof, opting instead for an implicit proof by survival.

currents running along the edge, but not inside the bulk of the sheet since the electrons there just move in circles. Also, the more tightly the electrons are squeezed against the edge, the higher their velocity.

The very same edge can also exhibit mechanical vibrations. In a solid material, there are many different types of waves [23, 24]. There are waves of longitudinal motion —sometimes called “compression waves” —there are waves with vibrations perpendicular to the direction of propagation —transverse waves (imagine a wave on a string) —and there are more complicated waves which move along the surfaces of objects: *surface acoustic waves*[5]. If we assume that the graphene sheet does not vibrate out of plane but remains perfectly flat, it can be seen as a two-dimensional solid with the edge its one-dimensional surface. Therefore, there are surface (or *edge*) waves propagating along the edge. Naturally, the edge being deformed by vibrations affects the electrons there. In the skipping-orbit picture described above, imagine the edge against which the electrons bounce being deformed, altering *how* the electrons bounce against it. Reciprocally, the electron collisions also affect the mechanical vibrations (see cover). The edge electrons and the acoustic edge waves *interact* with each other.

This thesis considers this interaction quantum-mechanically, and shows that, when parameters such as the magnetic field strength, the frequency of mechanical vibration and an applied voltage meet certain conditions, this interaction becomes significant. It is discovered in paper I that the interaction with electrons can cause low-amplitude mechanical vibrations to die out. In paper II it is then shown that, for higher-amplitude vibrations, the same effect can in some cases lead to the formation of acoustic *solitons*, localized waves which move with constant velocity without changing shape. These vibrational solitons can move with a speed greater than that of regular vibrational edge waves.

---

[5] These surface waves should come as no surprise to anyone familiar with earthquakes.

Chapter 2

Theory

The aim is to study the interaction between in-plane edge vibrations and magnetically induced electronic edge states in a graphene sheet. With this in mind, we consider the simplest possible system: a 2D semi-infinite graphene half-plane with a single edge running along the x-axis at $y = 0$. We will begin by describing the electronic subsystem, then the mechanical, and finally connect the two with a model for the interaction.

2.1 The Electronic Subsystem

Ultimately, the graphene sheet will be treated as a continuous elastic medium, so we are not interested in details on the atomic level. However, the standard electronic theory of graphene is based on the underlying honeycomb lattice structure. It is in fact the hexagonal symmetry of the lattice which gives rise to the special electronic behavior [13, 7]. Therefore, we will begin this chapter at the atomic level and build up the constituents of the theory, then gradually "zoom out" to a larger length scale in which the details of the lattice structure are obscured.

2.1.1 The Low-Energy Hamiltonian

The standard description of electrons in graphene starts out from a tight-binding model for the honeycomb lattice. It is then seen in the spectrum that low-energy properties are well described by an effective model in which the Schrödinger equation has a form reminiscent of the 2D Dirac equation describing relativistic fermions, with the mass put to zero [13, 25]. To derive this Hamiltonian, we begin by discussing the lattice itself.

Without any edge or magnetic field, let us simply consider an infinite graphene sheet, or rather, say we are considering a point so far from any edge that the sheet may be viewed as infinite. A graphene sheet consists of a 2D hexagonal honeycomb lattice of atomic bonds, where each vertex is occupied by a carbon atom. Thus each carbon atom is bonded to three neighboring atoms, and it has one electron to spare after bonding, that of the $2\mathrm{p}_z$-orbital; these unbonded electrons are the dominant contribution to transport properties [7]. In the hexagonal lattice, there are two inequivalent atoms in each unit cell, A and B [13, 7]. The lattice formed by all the A-atoms (B-atoms) is called the A-sublattice (B-sublattice). It must be stressed that the honeycomb lattice itself is *not* a Bravais lattice, rather, we will choose the A-sublattice as the Bravais lattice and include the B-atoms via a two-atom basis. We define lattice vectors for sublattice A and nearest-neighbor vectors linking the two sublattices as in Fig. 2.1a. The lattice vectors are

$$\mathbf{a}_1 = a\left(-\frac{1}{2}, -\frac{\sqrt{3}}{2}\right), \quad \mathbf{a}_2 = a\left(\frac{1}{2}, -\frac{\sqrt{3}}{2}\right), \tag{2.1}$$

where $a = 2.46$ Å is the lattice constant [13, 7], and the vectors from an A-atom to its nearest neighbors are

$$\boldsymbol{\delta R}_1 = a\left(0, \frac{1}{\sqrt{3}}\right), \boldsymbol{\delta R}_2 = a\left(-\frac{1}{2}, -\frac{1}{2\sqrt{3}}\right), \boldsymbol{\delta R}_3 = a\left(\frac{1}{2}, -\frac{1}{2\sqrt{3}}\right). \tag{2.2}$$

The reciprocal lattice vectors are

$$\mathbf{b}_1 = \frac{2\pi}{a}\left(-1, -\frac{1}{\sqrt{3}}\right), \quad \mathbf{b}_2 = \frac{2\pi}{a}\left(1, -\frac{1}{\sqrt{3}}\right), \tag{2.3}$$

and the reciprocal lattice is hexagonal, but rotated 90° with respect to the real lattice (Fig. 2.1b).

Each carbon atom in the lattice has one unhybridized orbital, the $2\mathrm{p}_z$-orbital, associated with the free electron of that atom. We take these orbitals to be normalized and neglect any overlap between orbitals belonging to different atoms, so that the set of all such $2\mathrm{p}_z$-orbitals can be used as a tight-binding orthonormal basis. We define the ket $|2\mathrm{p}_z, \mathbf{R}\rangle$ as the atomic

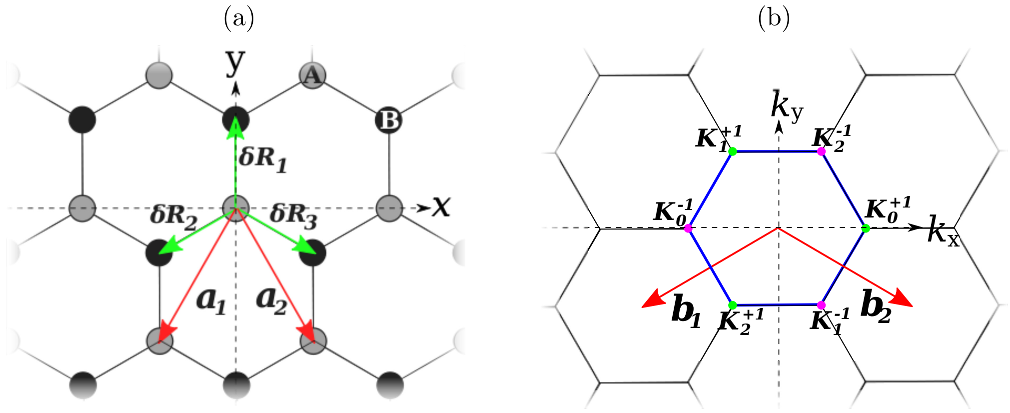

Figure 2.1: **(a)** The real-space lattice of graphene. There are two atoms per unit cell, labeled A (grey) and B (black). The A-sublattice lattice vectors are $\mathbf{a}_1$ and $\mathbf{a}_2$ (red) and each A-atom has three neighboring B-atoms, with nearest-neighbor vectors $\boldsymbol{\delta R}_n$, $n = 1, 2, 3$ (green). **(b)** The reciprocal lattice of graphene. The reciprocal lattice vectors are $\mathbf{b}_1$ and $\mathbf{b}_2$ (red) and the points at the corners of the first Brillouin zone (blue hexagon) are labeled $\mathbf{K}_\sigma^{(\tau)}$, with $\sigma = 0, 1, 2$ corresponding to a pair of inequivalent points $\tau = +1$ (green) and $\tau = -1$ (magenta).

2p$_z$-orbital of the carbon atom at lattice site $\mathbf{R}$. If we consider only interaction between nearest neighbors[1], we can write a tight-binding single-electron Hamiltonian in this basis as

$$\hat{H} = \sum_{\mathbf{R}_A}^{N} \sum_{n=1}^{3} -t_n \left|\mathbf{R}'_A + \boldsymbol{\delta R}_n\right\rangle \left\langle 2\mathrm{p}_z, \mathbf{R}_A\right| + \text{h.c.}, \tag{2.4}$$

where $-t_n$ is the hopping energy between nearest neighbors [13, 7] and N is the number of unit cells. There are no diagonal matrix elements of the form $\langle 2\mathrm{p}_z, \mathbf{R}| \hat{H} |2\mathrm{p}_z, \mathbf{R}\rangle$; they are equal to the energy of the 2p$_z$-orbital, which we put to zero by choosing it as our reference energy.

We now introduce a tight-binding basis set of Bloch functions for the

---

[1] We will justify the nearest-neighbor approximation and neglecting the orbital overlap later in the section.

single-electron state:

$$|A,\mathbf{k}\rangle = \frac{1}{\sqrt{N}}\sum_{\mathbf{R}_A}^{N} e^{i\mathbf{k}\cdot\mathbf{R}_A}\,|2\mathrm{p}_z,\mathbf{R}_A\rangle\,,$$

$$|B,\mathbf{k}\rangle = \frac{1}{\sqrt{N}}\sum_{\mathbf{R}_A}^{N}\sum_{n=1}^{3} e^{i\mathbf{k}\cdot(\mathbf{R}_A+\boldsymbol{\delta R}_n)}\,|2\mathrm{p}_z,\mathbf{R}_A+\boldsymbol{\delta R}_n\rangle\,. \tag{2.5}$$

Using these definitions, the Hamiltonian in Eq. (2.4) becomes

$$\hat{H} = \sum_{\mathbf{k}} F(\mathbf{k})\,|B,\mathbf{k}\rangle\,\langle A,\mathbf{k}| + \text{h.c.}, \tag{2.6}$$

where we defined

$$F(\mathbf{k}) \equiv \sum_{n=1}^{3} -t_n e^{-i\mathbf{k}\cdot\boldsymbol{\delta R}_n}. \tag{2.7}$$

We assume that the hopping energy between nearest-neighbors does not depend on the direction and write $t_1 = t_2 = t_3 \equiv t$. The hopping energy parameter is commonly taken as $t \approx 3$ eV [13, 7, 9].

The Hamiltonian is easily diagonalized and we find that the energy spectrum is given by [13, 7]

$$E_\pm(\mathbf{k}) = \pm|F(\mathbf{k})|t. \tag{2.8}$$

The "±" corresponds to two energy bands, the valence and the conduction band (Fig. 2.2). Given Born-von-Karman boundary conditions [1], the number of states in a band is equal to twice (due to spin) the number of unit cells in the lattice. In graphene, there are two free electrons per unit cell, one per carbon atom, and thus we find that in the ground state, the valence band is completely filled and the conduction band is completely empty. The two bands touch at the corners of the first Brillouin zone (Fig. 2.2). We denote these points $\mathbf{K}_\sigma^{(\tau)}$ where $\tau = \pm 1$ labels opposite corners, and $\sigma = 0, 1, 2$ labels the three pairs of opposite corners (Fig. 2.1b). For low energies, around $E < 2-3$ eV, i.e. a temperature on the order of 10^4 K, the electronic system is well described in the vicinty of these points, so we construct an effective model [13, 9] for the case of low electronic energies by expanding the function $F(\mathbf{k})$ to first order, $\mathbf{k} = \mathbf{K}_\sigma^{(\tau)} + \mathbf{k}'$,

$$F(\mathbf{k}) \approx \sum_{n=1}^{3} -te^{-i\mathbf{K}_\sigma^{(\tau)}\cdot\boldsymbol{\delta R}_n}(1 - i\mathbf{k}'\cdot\boldsymbol{\delta R}_n). \tag{2.9}$$

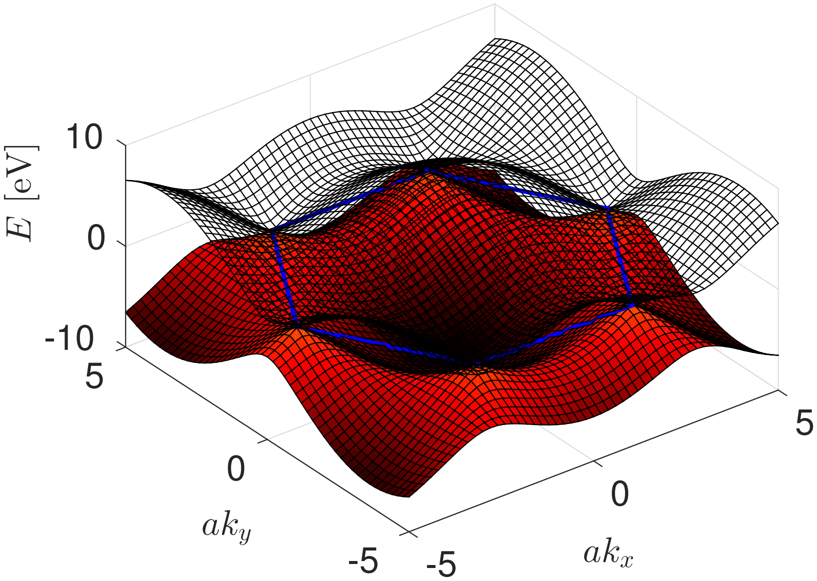

Figure 2.2: The nearest-neighbor tight-binding energy spectrum of graphene with $\epsilon_{2\mathrm{p}} = 0$, hopping energy $t = 3$ eV and zero atomic wave function overlap. In the ground state, the conduction band (transparent mesh) is completely empty and the valence band (orange-red) is completely filled. The two bands touch at the corners of the hexagonal first Brillouin zone (blue) as defined in Fig. 2.1b.

The small parameter in this expansion is $|\mathbf{k}'|a$, so this amounts to the continuum limit where the lattice constant is small compared to the wavelength. We now drop the prime on $\mathbf{k}'$ and simply measure $\mathbf{k}$ from the closest point $\mathbf{K}_\sigma^{(\tau)}$. Points $\mathbf{K}_\sigma^{(\tau)}$ of the same τ can be shown to differ from each other by a reciprocal lattice vector, and are thus equivalent, so we consider only one such pair of opposite points, commonly called the K-point ($\tau = +1$) and the K'-point ($\tau = -1$). We expect that the spectrum will be independent of our choice of σ. Considering the geometry of the reciprocal lattice (Fig. 2.1b) and using Eqs. (2.9) and (2.2), we get a low-energy Hamiltonian for the K-K' pair denoted by σ [13, 9],

$$\hat{H}_\sigma = \sum_{\tau=\pm1} e^{-i\tau\sigma\frac{2\pi}{3}} \hbar v_F \tau (k_x + i\tau k_y) \left|B, \mathbf{k}, \sigma, \tau\right\rangle \left\langle A, \mathbf{k}, \sigma, \tau\right| + \text{h.c.}, \tag{2.10}$$

where we used that $\tau^2 = 1$ and introduced (what will be seen to be) the Fermi velocity of graphene [13] as

$$\frac{at\sqrt{3}}{2\hbar} \equiv v_F \approx 10^6 \text{ m/s}. \tag{2.11}$$

Considering different pairs of points σ merely introduces a phase factor which does not affect the spectrum, as was expected. We arbitrarily choose the pair $\sigma = 0$ and suppress the index. This corresponds to the points $\mathbf{K}^{(\tau)} = (\tau K_x, 0)$. As a matter of preference, we also make the unitary transformation $\hat{U}\hat{H}\hat{U}^\dagger \equiv \hat{H}_{\text{el}}$, where

$$\hat{U} = \sum_{\tau=\pm 1} |A, \mathbf{k}, \tau\rangle \langle A, \mathbf{k}, \tau| + \tau\, |B, \mathbf{k}, \tau\rangle \langle B, \mathbf{k}, \tau| \,. \tag{2.12}$$

The K- and K'-points are not coupled and can be treated separately, $\hat{H}_{\text{el}} = \sum_\tau \hat{H}_{\text{el}}^{(\tau)}$. The Schrödinger equation for the point K/K' ($\tau = +1/-1$) can then be written

$$\hbar v_F \begin{pmatrix} 0 & k_x - i\tau k_y \\ k_x + i\tau k_y & 0 \end{pmatrix} \begin{pmatrix} \psi_A^{(\tau)}(\mathbf{k}) \\ \tau\psi_B^{(\tau)}(\mathbf{k}) \end{pmatrix} = E \begin{pmatrix} \psi_A^{(\tau)}(\mathbf{k}) \\ \tau\psi_B^{(\tau)}(\mathbf{k}) \end{pmatrix}, \tag{2.13}$$

$$\boldsymbol{\psi}_{(\tau)}(\mathbf{k}) \equiv (\psi_A^{(\tau)}(\mathbf{k}), \tau\psi_B^{(\tau)}(\mathbf{k}))^T.$$

The electronic states are now described by two-component vectors, $\boldsymbol{\psi}_{(\tau)}(\mathbf{k})$, called *pseudospinors* for their resemblance to usual spinors. However, the components indicate the sublattice, not spin. Note that $\mathbf{k}$ is always measured from the point in question, and that $\psi_A^{(\tau)}(\mathbf{k})$ and $\psi_B^{(\tau)}(\mathbf{k})$ are the components of the wave function in the basis given by Eq. (2.5).

The spectrum in this effective model is, for both K and K',

$$E_\pm^{(\tau)}(\mathbf{k}) = \pm\hbar v_F |\mathbf{k}|, \quad \tau = \pm 1, \tag{2.14}$$

i.e. two mirrored cones on top of each other [7], with coinciding zero-energy apexes at the K-point (K'-point) (Fig. 2.3). The spectrum around the K-point (K'-point) is sometimes referred to as the *K-valley* (*K'-valley*), a spectrum of this kind is known as a *Dirac cone*, and the point where the cones touch is called a *Dirac point*. The vanishing density of states at the Dirac point has lead to graphene being labeled a “zero-gap semiconductor” [26, 11]. It is remarkable that Eq. (2.13) is identical to the 2D Dirac equation for

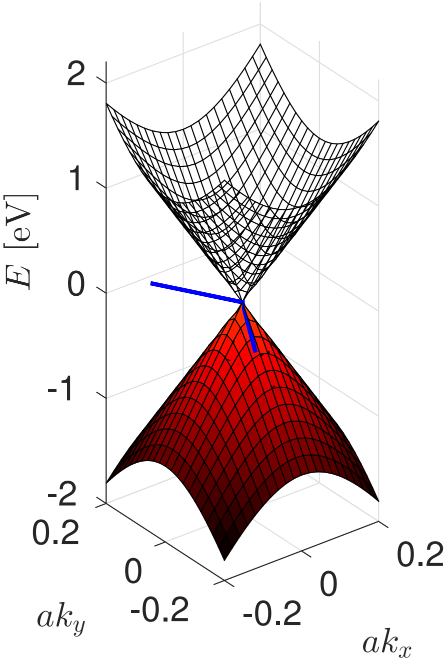

Figure 2.3: The effective-model (low-energy) spectrum of graphene around a K- or K-point, at a corner of the first Brillouin zone (blue), cf. Figs. 2.2 and 2.1b.

massless fermions [25], but with the speed of light replaced by v_F [13], the Fermi velocity[2].

In deriving Eq. (2.13) we neglected the overlap of atomic orbitals and kept only nearest-neighbor interaction. It can be shown that both the overlap and the second-nearest-neighbor interaction enters into the spectrum to second order in $|\mathbf{k}|$ [9], so in this regard, neglecting the overlap and the second-nearest-neighbor interaction is subsumed by the approximation made in doing a linear expansion in $\mathbf{k}$. In addition, the second-nearest-neighbor interaction introduces a constant energy shift on the order of the associated hopping energy. This hopping energy is however at least an order of magnitude lower than t [13]. Moreover, since we will eventually consider only a

---

[2] This is a crucial point. Too often in popular science writing are electrons in graphene described as “moving with the speed of light”. However, it is not the *speed* that is similar to relativistic particles ($v_F \ll c$), but the shape of the spectrum.

narrow energy region near a finite chemical potential, such an energy shift can be compensated for by adjusting the gate voltage.

We now have a Hamiltonian for the electronic subsystem which in itself makes no reference to the lattice structure. The pseudospinor components are envelope functions for the tight-binding Bloch functions corresponding to the two inequivalent sublattices, and we express the components with a continuous position variable, neglecting the fact that the A- and B-atoms are in different positions. In our continuum model, the sheet is continuous and at each position $\mathbf{r} = (x, y)$ the wave function has both an A- and a B-component. The Hamiltonian in Eq. (2.13) is often used as a starting point in calculations without reference to the underlying lattice structure in the cases where the discreteness of the lattice can be safely neglected [27, 28, 29].

We conclude this subsection by noting that the electronic Hamiltonian can be rewritten in terms of sublattice-space Pauli matrices $\boldsymbol{\sigma}_i$ as

$$\hat{\boldsymbol{H}}_{\text{el}}^{(\tau)} = v_F(\boldsymbol{\sigma}_x \hat{p}_x + \tau \boldsymbol{\sigma}_y \hat{p}_y), \tag{2.15}$$

where we took $\hbar k_i \to \hat{p}_i$.

2.1.2 The Zigzag Edge

We have so far only considered an infinite sheet. To introduce an edge into our system, we must construct suitable electronic boundary conditions. As was the case for the electronic Hamiltonian, the electronic boundary conditions are derived from the lattice structure.

In theoretical graphene physics we typically neglect the disordered and uneven edges of real graphene sheets, and distinguish between only two types: zigzag and armchair edges [13]. Here we will consider the graphene half-plane to be bounded by a zigzag edge of B-atoms along the x-axis at $y = 0$ (Fig. 2.4). All atoms on the zigzag edge belong to the B-sublattice, so at the edge the electronic wave function must vanish on the “missing” A-sublattice, meaning that the effective-model pseudospinor A-component must be zero. Considering the (position-space) wave function, the electronic boundary condition is [30, 13, 28]

$$\Psi_A(x, y)(x, 0) = e^{iK_x x}\psi_{A,+1}(x, 0) + e^{-iK_x x}\psi_{A,-1}(x, 0) = 0, \tag{2.16}$$

which includes terms from both Dirac points. Since the system is transla-

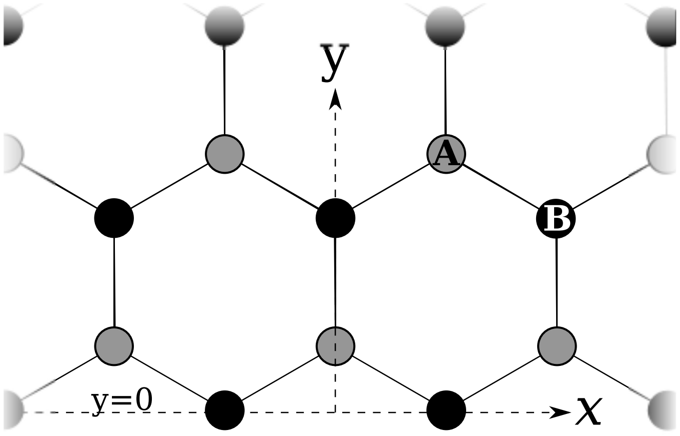

Figure 2.4: A graphene zigzag edge of B-atoms (black) along the x-axis at $y = 0$. At the edge, there are no A-atoms (grey), hence the wave function should vanish on the A-sublattice.

tionally invariant along x, we must have

$$\boldsymbol{\psi}_{\tau,k_x}(x,y) = e^{ik_x x}\begin{pmatrix}\phi_{A,k,\tau}(y)\\ \phi_{B,k,\tau}(y)\end{pmatrix}, \tag{2.17}$$

which, together with Eq. (2.16), means that we must have

$$\phi_{A,k,\tau}(0) = 0, \quad \tau = \pm 1. \tag{2.18}$$

Eq. (2.18) is the electronic boundary condition of our system: the pseudospinor A-component must vanish at the edge for both valleys separately. The fact that zigzag boundary conditions do not mix valleys means that the K- and K'-points can still be treated individually. This is in contrast to an armchair edge, which can be shown to mix valleys [30, 13, 28]. In fact, the edge was chosen as zigzag on account of this simplifying property.

2.1.3 Magnetically Induced Edge States

Here, we will derive the electronic spectrum and energy eigenfunctions in the presence of a magnetic field, perpendicular to the graphene half-plane, i.e.

$$\mathbf{B} = -B\mathbf{e}_z, \tag{2.19}$$

where $\mathbf{e}_z$ is the z-direction unit vector, normal to the sheet, and $B > 0$ (see cover). We represent this field by a vector potential in the Landau gauge,

$$\hat{\mathbf{A}}_B = B\hat{y}\mathbf{e}_x, \tag{2.20}$$

where $\hat{y}$ is the position operator for the coordinate y. We ignore spin, which we will comment on later, and simply introduce the vector potential into the electronic Hamiltonian of Eq. (2.15) via the minimal coupling $\hat{p} \to \hat{p}_i + e\hat{A}_i$ (the electron charge is $-e < 0$). In this way, the magnetic vector potential of Eq. (2.20) couples the position in the y-direction and the x-component of the momentum. We will eventually find that the energy eigenfunctions corresponding to large enough positive momentum in the x-direction are localized near the edge and have a finite velocity along it. This has a correspondence to the classical skipping orbits discussed in section 1.2, whose paths became straighter, thus gaining speed, when the y-position of the orbit center is moved further toward and even over the edge.

The magnetic field introduces a characteristic length scale into the system, the magnetic length

$$l_B \equiv \sqrt{\frac{\hbar}{|eB|}} \approx 26 \text{ nm}/\sqrt{B[T]}, \tag{2.21}$$

where $B[T]$ (dimensionless) is the magnetic field strength in Tesla. We use this length to nondimensionalize the problem by defining $\tilde{x} \equiv x/l_B$, $\tilde{k}_x \equiv l_B p_x$ and the analogous definitions for the y-coordinate. The scaled operators then obey the commutation relations

$$\left[\hat{\tilde{x}}, \hat{\tilde{k}}_x\right] = i, \quad \left[\hat{\tilde{y}}, \hat{\tilde{k}}_y\right] = i. \tag{2.22}$$

Similarily, we define a dimensionless energy as

$$\tilde{E} = \frac{E}{E_B}, \quad E_B \equiv \frac{\sqrt{2}\hbar v_F}{l_B}. \tag{2.23}$$

It will also prove useful to introduce the sublattice index σ, where $\sigma = +1$ indicates the pseudospinor A-component and $\sigma = -1$ the B-component, to represent many equations simultaneously[3], as well as highlight certain

---

[3] Note that this σ is not the same was that which was introduced in a previous subsection.

symmetries with the valley index τ. With these rescalings and definitions, Eq. (2.15) with the magnetic vector potential of Eq. (2.20) included can be written as two coupled equations,

$$(\hat{\tilde{k}}_x + \hat{\tilde{y}} + i\sigma\tau\hat{\tilde{k}}_y)\,\langle\sigma,\tau|\psi\rangle = \sqrt{2}\tilde{E}\,\langle-\sigma,\tau|\psi\rangle\,, \quad \sigma = \pm 1. \tag{2.24}$$

We now distinguish between two cases: energy $\tilde{E} = 0$ and $\tilde{E} \neq 0$. In the first case, the equations for the two components A and B decouple, while in the second case we may divide by $\tilde{E}$ to solve for one component and insert it into the other equation. We project the states into position space and note that due to translational invariance in the $\tilde{x}$-direction, the pseudospinor must be of the form of Eq. (2.17) with $\tilde{k}_x \equiv \tilde{k}$ a good quantum number, so the equations are now in the single variable $\tilde{y}$ with $\tilde{k}$ just a number.

For $\tilde{E} = 0$ we get the two decoupled equations

$$(\tilde{k} + \tilde{y} + \sigma\tau\partial_{\tilde{y}})\phi^{(\tau)}_{\sigma,k,\tilde{E}=0}(\tilde{y}) = 0, \quad \sigma = \pm 1. \tag{2.25}$$

which we try to solve using the Gaussian ansatz (we omit normalization until the end of this subsection)

$$\phi^{(\tau)}_{\sigma,k,\tilde{E}=0}(\tilde{y}) = e^{-\alpha(\tilde{k}+\tilde{y})^2}, \quad \alpha > 0. \tag{2.26}$$

Substituting, we find $\alpha = 1/2$ and see that we must have $\sigma = \tau$, which couples the sublattice and valley indices. We have thus found a solution for $\tilde{E} = 0$ in both valleys, but only the solution $\sigma = \tau = -1$ can fulfill the boundary condition in Eq. (2.18) so the solution in the K-valley must be rejected. Therefore the only $\tilde{E} = 0$ solution is

$$\tilde{E} = 0 \quad \sim \quad \boldsymbol{\psi}^{(-1)}_{\tilde{k},\tilde{E}=0}(\tilde{x},\tilde{y}) = e^{i\tilde{k}\tilde{x}} \begin{pmatrix} 0 \\ e^{-\frac{1}{2}(\tilde{k}+\tilde{y})^2} \end{pmatrix}. \tag{2.27}$$

Bizarrely, this solution satisfies the boundary condition *everywhere* and seemingly behaves as if there was no edge present. This zero-energy level has been the subject of several research papers [31, 32, 33, 27] and will not be discussed further in this thesis, as we will ultimately consider low-energy transitions where this state is far below a finite chemical potential and thus rendered inert.

We now return to Eq. (2.24) and consider the other case, $\tilde{E} \neq 0$. We solve one of the equations for the right-hand-side pseudospinor component and substitute it into the other equation, yielding the two coupled equations

$$\begin{aligned}((\tilde{k}+\tilde{y})^2-\partial_{\tilde{y}}^2-(2\tilde{E}^2+\sigma\tau))\phi^{(\tau)}_{\sigma,k,\tilde{E}\neq 0}(\tilde{y})&=0,\\ \frac{1}{\sqrt{2}\tilde{E}}(\tilde{k}+\tilde{y}+\sigma\tau\partial_{\tilde{y}})\phi^{(\tau)}_{\sigma,k,\tilde{E}\neq 0}(\tilde{y})&=\phi^{(\tau)}_{-\sigma,k,\tilde{E}\neq 0}(\tilde{y}),\end{aligned} \tag{2.28}$$

where it should be understood that $\sigma=+1$ *or* $\sigma=-1$, depending on which pseudospinor component we chose to solve for. We then consider the K-valley ($\tau=+1$) only. Choosing $\sigma=+1$ (i.e. we solved for the A-component), we get an equation for $\phi_{A,+1,k,\tilde{E}\neq 0}(\tilde{y})$ which we can write

$$\partial_\xi^2\phi^{(+1)}_{A,k,\tilde{E}\neq 0}(\xi)+(\nu+\frac{1}{2}-\frac{1}{4}\xi^2)\phi^{(+1)}_{A,k,\tilde{E}\neq 0}(\xi)=0 \tag{2.29}$$

where the new variable is $\xi=\sqrt{2}(\tilde{k}+\tilde{y})$ and $\nu=\tilde{E}^2$. Eq. (2.29) is a well-known equation, the independent solutions of which are the so-called *parabolic cylinder functions* $D_\nu(\xi)$ and $D_{-\nu-1}(i\xi)$, of which only the first goes to zero as $\xi\to+\infty$. We therefore find that $\phi^{(+1)}_{A,k,\tilde{E}\neq 0}(\tilde{y})=D_\nu(\sqrt{2}(\tilde{k}+\tilde{y}))$ (note that we omit normalization until the end of the subsection) [34, 29, 27, 35]. The other line in Eq. (2.28) gives us an expression for the other component,

$$\phi^{(+1)}_{B,k,\tilde{E}\neq 0}(\tilde{y})=\frac{1}{\tilde{E}}(\frac{1}{2}\xi+\partial_\xi)D_\nu(\xi). \tag{2.30}$$

Using the relation $(\partial_\xi+\xi/2)D_\nu(\xi)=\nu D_{\nu-1}(\xi)$ [34, 35] we get the B-component and thus the full pseudospinor solution in the K-valley,

$$\tilde{E}\neq 0 \quad\sim\quad \boldsymbol{\psi}^{(+1)}_{\tilde{k},\tilde{E}}(\tilde{x},\tilde{y})=e^{i\tilde{k}\tilde{x}}\begin{pmatrix}D_\nu(\sqrt{2}(\tilde{k}+\tilde{y}))\\ \sqrt{\nu}D_{\nu-1}(\sqrt{2}(\tilde{k}+\tilde{y}))\end{pmatrix}. \tag{2.31}$$

To find the solutions in the K'-valley, we note that σ and τ always appear as the product $\sigma\tau$, so when interchanging valleys, $\tau\to-\tau$, we can retain the form of the equations by also interchanging sublattices, $\sigma\to-\sigma$. We can therefore restart from Eq. (2.28) but now consider the K'-valley ($\tau=-1$) and compensate by instead choosing $\sigma=-1$ (meaning that we solved Eq. (2.24) for the B-component). We then find the same Eqs. (2.29) and (2.30) but with $\tau\to-1$ and $A\leftrightarrow B$, so in the K'-valley we find

$$\tilde{E}\neq 0 \quad\sim\quad \boldsymbol{\psi}^{(-1)}_{\tilde{k},\tilde{E}}(\tilde{x},\tilde{y})=e^{i\tilde{k}\tilde{x}}\begin{pmatrix}\sqrt{\nu}D_{\nu-1}(\sqrt{2}(\tilde{k}+\tilde{y}))\\ D_\nu(\sqrt{2}(\tilde{k}+\tilde{y}))\end{pmatrix}. \tag{2.32}$$

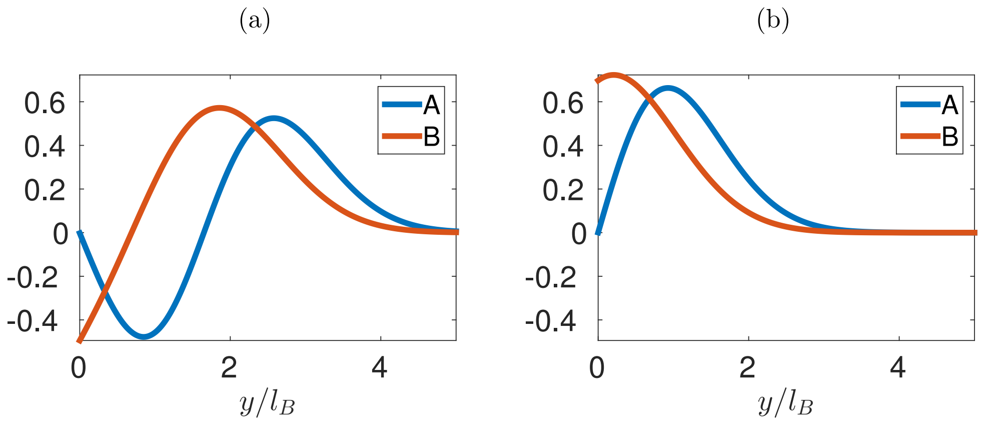

Figure 2.5: The A- and B-components of the (normalized) K-valley pseudospinor component $\boldsymbol{\phi}_\nu^{(+1)}(y/l_B)$ (see Eq. (2.37)), where $\nu = (1+\sqrt{2})/2$. The wave vector is $kl_B = -1.29$ **(a)** and $kl_B = 0.36$ **(b)**, respectively.

The energy is given in terms of ν, and by substituting the wave functions into the boundary condition of Eq. (2.18) we find equations for the spectrum. For the K-valley we find the allowed energies by solving

$$E_\nu^{(+1)}(\tilde{k}) = \pm\sqrt{\nu}, \quad D_\nu(\sqrt{2}\tilde{k}) = 0, \tag{2.33}$$

and for the K'-valley we instead solve

$$E_\nu^{(-1)}(\tilde{k}) = \pm\sqrt{\nu}, \quad D_{\nu-1}(\sqrt{2}\tilde{k}) = 0. \tag{2.34}$$

These equations can be solved numerically [36]; the resulting spectrum is plotted in Fig. 2.6 together with the dispersionless $\tilde{E} = 0$ level we found when deriving Eq. (2.27). Due to the quadratic dependence of ν on $\tilde{E}$, the spectrum is electron-hole symmetric. At large negative $\tilde{k}$, the allowed energies $\pm\sqrt{\nu}$ tend to $\pm\sqrt{n}$, n being an integer; the bands asymptotically approach dispersionless *Landau levels* [37, 13] and the functions $D_\nu(\xi)$ approach the energy eigenfunctions of the unconfined quantum harmonic oscillator [35, 38], centered at $\tilde{y} = -\tilde{k}$. These are localized wave functions with zero velocity, and cannot produce a current. In the classical skipping-orbit picture, this corresponds to electronic orbits with orbit center far from the edge. As $\tilde{k}$ increases, the orbit center moves toward and over the edge, and the energy levels become dispersive bands with a finite velocity along the edge. We

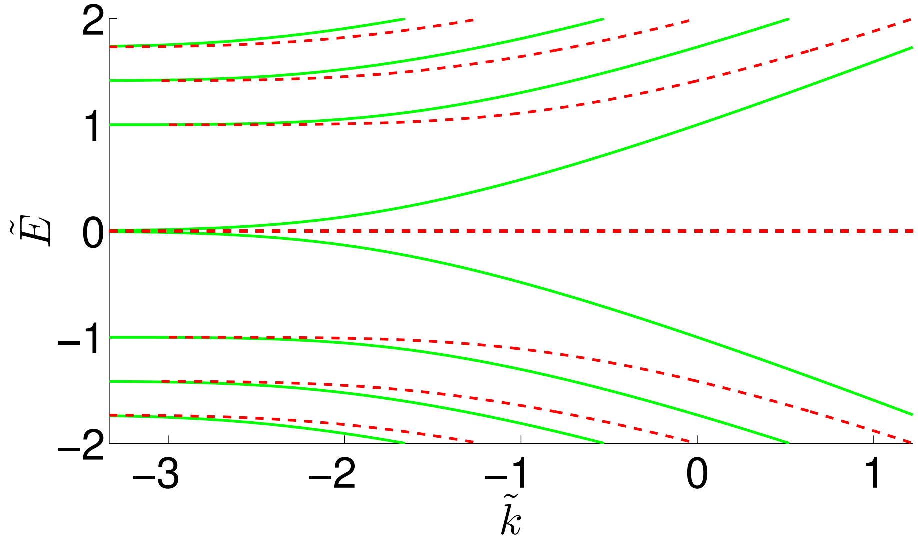

Figure 2.6: The nondimensionalized electronic spectrum for the considered system, with a zigzag edge and a perependicular magnetic field. The solid green (dashed red) lines are states in the K-valley (K'-valley). The K'-valley has a dispersionless level at $\tilde{E} = 0$ which effectively replaces the band missing due to the offset in the index between the pseudospinor A-components of the two valleys ($D_{\nu-1}(\xi)$ vs $D_\nu(\xi)$). The bands will be labeled according to their corresponding bulk Landau level, i.e. $\varkappa = +1$ ($\varkappa = -1$) for positive-energy (negative-energy) levels, and $n = 0, 1, 2, \ldots$ counted from $\tilde{E} = 0$.

therefore see a clear correspondence between the quantum mechanical and skipping-orbit results. The bulk Landau levels are commonly labeled by an integer n, starting from $n = 0$ at zero energy. We will use the index n to label the energy band whose energy approaches the energy of Landau level n as $\tilde{k} \to -\infty$. Another index, $\varkappa = \pm 1$, will denote the positive (+) and negative (-) energies.

We may then summarize the spectrum and energy eigenfunctions as

$$\begin{aligned} \tilde{E}^{(\tau)}_{\varkappa,n}(\tilde{k}) \quad \sim \quad \boldsymbol{\psi}^{(\tau)}_{\tilde{k},\varkappa,n}(\tilde{x},\tilde{y}) &= N^{(\tau)}_{\nu}(\tilde{k}) e^{i\tilde{k}\tilde{x}} \boldsymbol{\phi}^{(\tau)}_{\tilde{k},\nu}(\tilde{y}), \\ \nu &= \left(\tilde{E}^{(\tau)}_{\varkappa,n}(\tilde{k})\right)^2, \end{aligned} \tag{2.35}$$

where $N_\nu^{(\tau)}(k)$ is a normalization constant which ensures that

$$\iint \mathrm{d}x\,\mathrm{d}y\,\boldsymbol{\psi}^{(\tau)*}_{\tilde{k},\varkappa,n}(x/l_B, y/l_B)\cdot\boldsymbol{\psi}^{(\tau)}_{\tilde{k},\varkappa,n}(x/l_B, y/l_B) = 1. \tag{2.36}$$

Note that $-\infty < x < \infty$ but $0 \leq y < \infty$. The energies $\tilde{E}^{(\tau)}_{\varkappa,n}(\tilde{k})$ are presented in Fig. 2.6. The $\tilde{y}$-dependent vector part of the wave function is, in the K-valley:

$$\boldsymbol{\phi}^{(+1)}_{\tilde{k},\nu}(\tilde{y}) = \begin{pmatrix} D_\nu(\sqrt{2}(\tilde{k}+\tilde{y})) \\ \sqrt{\nu}D_{\nu-1}(\sqrt{2}(\tilde{k}+\tilde{y})) \end{pmatrix}. \tag{2.37}$$

In the K'-valley we have instead, for nonzero energies so that $\nu \neq 0$,

$$\boldsymbol{\phi}^{(+1)}_{\tilde{k},\nu}(\tilde{y}) = \begin{pmatrix} \sqrt{\nu}D_{\nu-1}(\sqrt{2}(\tilde{k}+\tilde{y})) \\ D_\nu(\sqrt{2}(\tilde{k}+\tilde{y})) \end{pmatrix}. \tag{2.38}$$

(As previously mentioned, we will not be considering the zero-energy states.) These are the energy eigenfunctions of the electronic Hamiltonian in the presence of a magnetic field. Returning to the unscaled variable, $y = \tilde{y}l_B$, we see that the wave functions are localized to edge on the order of the magnetic length (see Fig. 2.5).

The energy spacing between the bands is on the order of $E_B \approx 26$ meV $\cdot \sqrt{B[T]}$, corresponding to a temperature of 298 K $\cdot \sqrt{B[T]}$. In order to have distinct energy bands, the temperature must be much lower than this value. In comparison, the Zeeman splitting corresponds to a temperature of 0.67 K $\cdot\, B[T]$ [29]. Therefore, we may consider the bands as distinct and spin degenerate as long as the temperature T satisfies

$$0.67\text{ K}\cdot B[T] \ll T \ll 298\text{ K}\cdot\sqrt{B[T]}. \tag{2.39}$$

With this, we conclude the description of the electronic subsystem.

2.2 The Acoustic Subsystem

The vibrational motion of the graphene sheet will be modeled using the theory of elasticity. To do so is to treat the sheet as a completely continuous medium, ignoring all details on the atomic level. This requires that the separation between individual carbon atoms in the graphene sheet, which is on the order of single Ångströms [13], is much smaller than any other length scale we consider. For the acoustic (electronic) subsystem, that length scale is the acoustic wave length (the magnetic length). First we present a classical acoustic Hamiltonian, then we use it to derive the Rayleigh edge waves which are the object of study. Finally, we outline how to quantize the acoustic field and expand it in different types of waves.

2.2.1 The Acoustic Hamiltonian

The theory of elasticity, or continuum mechanics, deals with the behavior of continuous bodies in the framework of classical mechanics. Applying pressure, bending, stretching, or heating a solid, causes each tiny piece of the material in the body to be displaced from its equilibrium position. We describe this displacement by a 2D displacement field,

$$\mathbf{u}(\mathbf{r}) \equiv \mathbf{r}' - \mathbf{r}, \tag{2.40}$$

where $\mathbf{r} = (x, y)$ is the equilibrium position of an infinitesimal piece of material and $\mathbf{r}'$ is the displaced position [23]. A related quantity is the strain tensor, defined as $u_{ij} = (\partial_i u_j + \partial_j u_i)/2$. By modeling the sheet as a 2D medium, we have completely neglected flexural (out-of-plane) motion. By introducing a momentum $\boldsymbol{\pi}(\mathbf{r})$ conjugate to $\mathbf{u}(\mathbf{r})$, we can write a classical Hamiltonian [24] as[4]

$$H_{\text{ac}} = \iint \frac{\boldsymbol{\pi}^2(\mathbf{r})}{2\rho_{\text{gr}}} - \frac{\rho_{\text{gr}}}{2}\mathbf{u}(\mathbf{r}) \cdot \mathcal{L}\mathbf{u}(\mathbf{r})\,\mathrm{d}x\,\mathrm{d}y \tag{2.41}$$

where $\rho_{\text{gr}} = 7.6 \cdot 10^{-7}$ kg/m^2 is the 2D mass density of graphene [39], and $\mathcal{L}$ is an operator acting on $\mathbf{u}(\mathbf{r})$ defined as

$$\mathcal{L} = s_l^2\,\mathbf{grad}\;\mathrm{div} - s_t^2\,\mathbf{curl}\,\mathbf{curl} \tag{2.42}$$

where $s_l = 2.1 \cdot 10^4$ m/s and $s_t = 1.4 \cdot 10^4$ m/s are the longitudinal and transverse sound speeds in graphene [40]. Hamilton's equations then yield the equation of motion for $\mathbf{u}(\mathbf{r})$ as

$$\partial_t^2 \mathbf{u}(\mathbf{r}; t) = \mathcal{L}\mathbf{u}(\mathbf{r}; t). \tag{2.43}$$

The ith component of the right-hand side of this equation can be shown [24] to be equal to $\rho_{\text{gr}}^{-1}\partial_j \sigma_{ij}$, where σ_{ij} is the *stress tensor*, which describes the

---

[4] Note that the integration is over the half-plane: $-\infty < x < \infty$, $0 \leq y < \infty$.

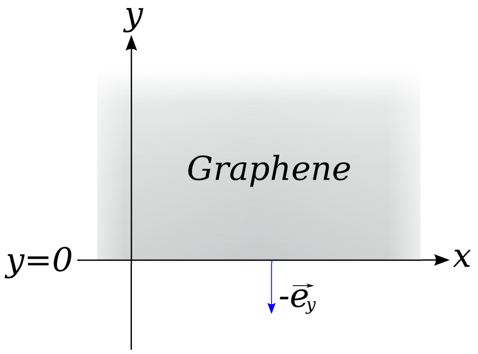

Figure 2.7: The graphene sheet is treated as a continuous 2D half-plane occupying $y \geq 0$. The edge is considered stress-free and the normal to the edge is the negative unit vector in the y-direction, $-\mathbf{e}_y$.

internal restorative forces generated by the strain [23]. Explicitly, the stress tensor can be written in terms of the strain tensor as [24]

$$\rho_{\text{gr}}\sigma_{ij}(\mathbf{r}) = (s_l^2 - 2s_t^2)u_{kk}(\mathbf{r})\delta_{ij} + 2s_t^2 u_{ij}(\mathbf{r}). \tag{2.44}$$

If we assume that the edge of the graphene sheet is free to vibrate and not subject to any external forces, the boundary condition is given in terms of the stress tensor as

$$\sum_{j=x,y} \sigma_{ij}(x,0)n_j = 0, \quad i = x, y, \tag{2.45}$$

where $\mathbf{n} = -\mathbf{e}_y$ is a unit vector normal to the edge (Fig. 2.7) [23].

The displacement field $\mathbf{u}(\mathbf{r};t)$ can, like any vector field, be separated into the sum of a zero-divergence field and a zero-curl field, which we will call $\mathbf{u}_l(\mathbf{r};t)$ and $\mathbf{u}_t(\mathbf{r};t)$, respectively. By doing this in Eq. (2.43) and taking the curl and divergence of the full equation, we arrive at two wave equations [23],

$$\partial_t^2 \mathbf{u}_i(\mathbf{r};t) = s_i^2 \nabla^2 \mathbf{u}_i(\mathbf{r};t), \quad i = l, t. \tag{2.46}$$

The displacements $\mathbf{u}_l(\mathbf{r};t)$ and $\mathbf{u}_t(\mathbf{r};t)$ are said to describe longitudinal and transverse waves. “Longitudinal” (“transverse”) is here meant in the sense of having zero curl (divergence). In the case of an infinite medium, the two wave equations are uncoupled and the longitudinal and transverse waves propagate independently. However, the introduction of an edge via the boundary condition of Eq. (2.45) couples the two fields so that only certain linear combinations of longitudinal and transverse motion are possible. This leads to the appearance of different types of waves in a system.

2.2.2 Rayleigh Waves

Infinitely far from the edge, at $y \to \infty$, the solutions to the equations of motion must either approach those of the infinite-bulk system (plane waves) or simply disappear. In the latter case, the solutions are localized to the vicinity of the edge. We will here seek such solutions, and the solutions we find are called *Rayleigh waves*, a well known type of surface wave. Since Rayleigh waves oscillate in the plane spanned by the surface normal and the propagation direction, they are 2D objects even in 3D systems, and typically the 3D Rayleigh-wave solutions are found by a 2D calculation which neglects the third dimension due to symmetry [23, 41, 24]. However, our system is *actually* 2D and the "surface" is the edge of the graphene sheet.

Since the calculations will involve only linear operations on the displacement field, we choose to work with complex fields $\bar{\mathbf{u}}$, knowing that we can eliminate the imaginary part at the end of calculations. We consider fields with a harmonic time dependence, $\exp(-i\omega t)$, and the translational invariance in the x-direction immediately implies an x-dependent factor $\exp(iqx)$, with q the wave vector x-component. Since we seek localized solutions, we assume that the y-dependent part of the displacement field vanishes into the bulk. I.e. we have

$$\bar{\mathbf{u}}_i(x, y; t) = \bar{\mathbf{u}}_i(x, y)e^{-i\omega t} = \mathbf{f}_i(y)e^{i(qx-\omega t)}, \quad i = l, t \tag{2.47}$$

which, when inserted into Eq. (2.46), yields

$$\partial_y^2 \mathbf{f}_i(y) = \left(q^2 - \frac{\omega^2}{s_i^2}\right)\mathbf{f}_i(y), \quad i = l, t. \tag{2.48}$$

The localized solution of which is

$$\mathbf{f}_i(y) = \mathbf{A}_i e^{-\kappa_i y}, \quad i = l, t \tag{2.49}$$

where $\mathbf{A}_i$ is a constant vector, and

$$\kappa_i = \sqrt{q^2 - \frac{\omega^2}{s_i^2}}, \quad i = l, t, \tag{2.50}$$

is a real number which determines the magnitude of decay into bulk of the waves, i.e. the localization to the edge. Note that the transverse and longitudinal components have different degrees of localization since $\kappa_t \neq \kappa_l$; this is a general feature of Rayleigh waves [23, 41]. The localization also depends on q. Since $\bar{\mathbf{u}}_l(\mathbf{r})$ ($\bar{\mathbf{u}}_t(\mathbf{r})$) has zero curl (divergence), we must have

$$\frac{A_{t,y}}{A_{t,x}} = \frac{iq}{\kappa_t}, \quad \frac{A_{l,y}}{A_{l,x}} = \frac{i\kappa_l}{q}. \tag{2.51}$$

The boundary condition of Eq. (2.45) gives the ratio

$$\frac{A_{l,x}}{A_{t,x}} = -\frac{\kappa_t^2 + q^2}{2\kappa_l \kappa_t}. \tag{2.52}$$

and the equation

$$s_t^2 \frac{\kappa_t^2 + q^2}{2\kappa_l \kappa_t} \left(\frac{\kappa_l^2}{q^2} - 1 \right) + s_t^2 \left(\frac{\kappa_t^2 + q^2}{\kappa_l \kappa_t} - 2 \right) = 0 \tag{2.53}$$

Thus the edge connects the longitudinal and transverse fields. Eqs. (2.51) and (2.52) can eliminate three of the four constants $A_{i,j}$ ($i = l, t,\ j = x, y$); the overall amplitude u_0 is not specified by the theory. Eq. (2.53) relates q to ω (throught κ_l and κ_t) and will thus lead to a dispersion relation. Making the ansatz of a linear dispersion, $\omega(q) = \zeta s_t |q|$, creates a fourth-degree equation in the unknown ζ, which we solve numerically. In order for ω, κ_l and κ_t to be real, we must have ζ real and $0 < \zeta < 1$. These restrictions leave only one root, $\zeta \approx 0.89$. This leads to the dispersion relation for 2D Rayleigh waves,

$$\omega_R(q) = s_R |q|, \tag{2.54}$$

where $s_R \equiv \zeta s_t = 1.2 \cdot 10^4$ m/s is the speed of sound of such waves and we introduced the index R for "Rayleigh". We define constants λ_t and λ_l in terms of ζ such that that $\kappa_i = \lambda_i |q|$, and rewrite the (complex) displacement field as

$$\bar{\mathbf{u}}_{R,q}(x, y) = u_0\, \mathbf{f}_q(y) e^{iqx}, \tag{2.55}$$

with

$$\mathbf{f}_q(y) = \begin{pmatrix} e^{-\lambda_l |q| y} - C_x e^{-\lambda_t |q| y} \\ -i\, \mathrm{sgn}(q) \left(-\lambda_l e^{-\lambda_l |q| y} + C_y e^{-\lambda_t |q| y} \right) \end{pmatrix}, \tag{2.56}$$

where we appended q as an index [23, 41]. The constants introduced all depend on the ratio s_l/s_t only (or equivalently, on the Poisson ratio [23]) and are close to unity. Specifically, we find

$$\begin{aligned}\lambda_l &= \sqrt{1-\zeta^2} \approx 0.81, \\ \lambda_t &= \sqrt{1-(s_t/s_l)^2\zeta^2} \approx 0.46, \\ C_x &= \frac{2\lambda_l\lambda_t}{\lambda_t^2+1} \approx 0.61, \\ C_y &= \frac{C_x}{\lambda_t} \approx 1.3.\end{aligned} \tag{2.57}$$

We can make the displacement field real by adding the complex conjugate of the complex field (now including the harmonic time dependence),

$$\begin{aligned}\mathbf{u}_{R,q}(x,y;t) \equiv \bar{\mathbf{u}}_{R,q}(x,y)e^{-i\omega_R(q)t} + \bar{\mathbf{u}}^*_{R,q}(x,y)e^{i\omega_R(q)t} = \\ = 2u_0 \begin{pmatrix} \left(e^{-\lambda_l|q|y} - C_x e^{-\lambda_t|q|y}\right)\cos(q[x-s_Rt]) \\ \operatorname{sgn}(q)\left(-\lambda_l e^{-\lambda_l|q|y} + C_y e^{-\lambda_t|q|y}\right)\sin(q[x-s_Rt]) \end{pmatrix}.\end{aligned} \tag{2.58}$$

The Rayleigh waves move slower than bulk waves, $s_R < s_t < s_l$, and there is a phase difference between the x- and y-components. The waves take the shape of a “rolling” in-plane motion propagating along the edge (Fig. 2.8) and the motion is retrograde near the edge but prograde further into the bulk. The higher the frequency, the more strongly localized they are to the edge; the penetration depth of the waves into the bulk sheet is on the order of the wavelength.

2.2.3 Quantization

To quantize the acoustic subsystem, we can simply replace the displacement field and its conjugate momentum with operators, $\hat{\mathbf{u}}(\mathbf{r})$ and $\hat{\boldsymbol{\pi}}(\mathbf{r})$, which obey the canonical commutation relation $[\hat{u}_i(\mathbf{r}), \hat{\pi}_j(\mathbf{r}')] = i\hbar\delta(\mathbf{r}-\mathbf{r}')\delta_{ij}$. The Hamiltonian (cf. Eq. (2.41)) is then simply

$$\hat{H}_{\text{ac}} = \iint \frac{\hat{\boldsymbol{\pi}}^2(\mathbf{r})}{2\rho_{\text{gr}}} - \frac{\rho_{\text{gr}}}{2}\hat{\mathbf{u}}(\mathbf{r})\cdot\mathcal{L}\hat{\mathbf{u}}(\mathbf{r})\,\mathrm{d}x\,\mathrm{d}y\,, \tag{2.59}$$

and the equations of motions in the Heisenberg picture replicate the classical equations of motion, Eq. (2.43). However, eventually we will consider only Rayleigh waves of specific wave vectors. For this reason will we now proceed to describe an expansion of the fields $\hat{\mathbf{u}}(\mathbf{r})$ and $\hat{\boldsymbol{\pi}}(\mathbf{r})$ in different wave types

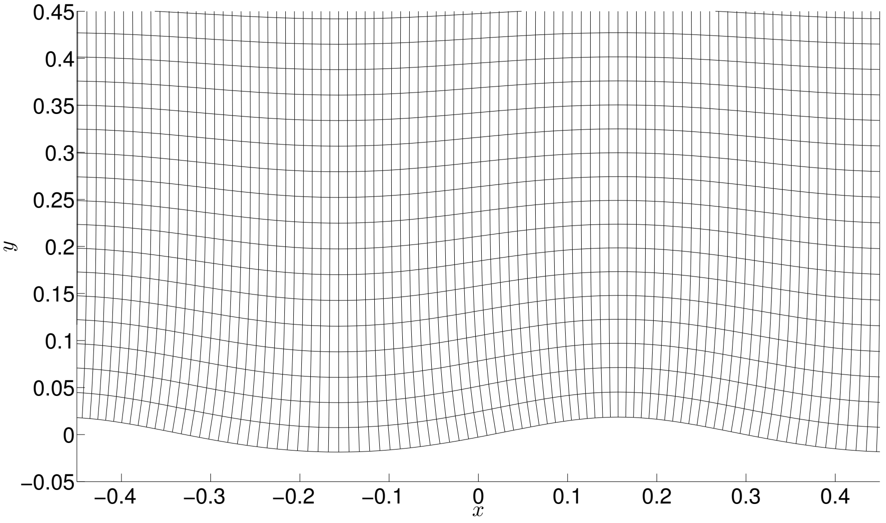

Figure 2.8: A snapshot of Rayleigh waves along an edge (at $y = 0$). The displacement field is according to Eqs. (2.55) and (2.56), with arbitrary units.

and wave vectors. We will begin the description of this expansion with the classical fields, $\mathbf{u}(\mathbf{r})$ and $\boldsymbol{\pi}(\mathbf{r})$, and then introduce quantization.

We will be expanding the two fields in a complete basis of "eigenwaves" and then show that the canonical commutation relation implies that the expansion coefficients are creation and annihilation operators of phonons [24]. We once again work with complex fields $\bar{\mathbf{u}}$, and begin by noting that if we consider only fields with a harmonic time dependence, $\bar{\mathbf{u}}(\mathbf{r};t) = \bar{\mathbf{u}}_J(\mathbf{r})\exp(-i\omega_J t)$, Eq. (2.43) becomes an eigenvalue equation,

$$-\omega_J^2 \bar{\mathbf{u}}_J(\mathbf{r}) = \mathcal{L}\bar{\mathbf{u}}_J(\mathbf{r}). \tag{2.60}$$

We define the space of complex fields $\bar{\mathbf{u}}_J(\mathbf{r})$ (where J is only a symbolic index[5].) which satisfy the boundary condition of Eq. (2.45), and equip this space with the inner product

$$\langle \bar{\mathbf{u}}(\mathbf{r}), \bar{\mathbf{v}}(\mathbf{r})\rangle \equiv \iint \bar{\mathbf{u}}^*(\mathbf{r})\cdot\bar{\mathbf{v}}(\mathbf{r})\,\mathrm{d}x\,\mathrm{d}y\,, \tag{2.61}$$

where the integration is over the half-plane $y \geq 0$. It can be shown, using integration by parts and Eq. (2.45), that $\langle \bar{\mathbf{u}}(\mathbf{r}), \mathcal{L}\bar{\mathbf{v}}(\mathbf{r})\rangle = \langle \mathcal{L}\bar{\mathbf{u}}(\mathbf{r}), \bar{\mathbf{v}}(\mathbf{r})\rangle$, i.e.

---

[5] Summation over J may even imply integration over continuous labels.

$\mathcal{L}$ is a Hermitian operator in this space [24]. Therefore, we can use the "eigenwaves" of $\mathcal{L}$ to construct a complete orthonormal basis $\{\bar{\mathbf{u}}_J(\mathbf{r})\}$. We can then expand any displacement field in this basis,

$$\mathbf{u}(\mathbf{r}) = \sum_J \sqrt{\frac{\hbar}{2\rho_{\mathrm{gr}}\omega_J}} \left(b_J \bar{\mathbf{u}}_J(\mathbf{r}) + b_J^* \bar{\mathbf{u}}_J^*(\mathbf{r}) \right), \tag{2.62}$$

where we added the conjugate term to make the field real, and the parenthesis prefactor has been factored out of the expansion coefficients $b_J^{(*)}$. We find the corresponding expression for the conjugate momentum by first attaching the harmonic time-dependencies $\exp(-i\omega_J t)$ to the terms $\bar{\mathbf{u}}_J(\mathbf{r})$, and analogously for the conjugate terms; this gives us an expansion of the time-dependent field $\mathbf{u}(\mathbf{r};t)$. We then insert that expansion into Hamilton's equation, $\rho_{\mathrm{gr}}\partial_t \mathbf{u}(\mathbf{r};t) = \boldsymbol{\pi}(\mathbf{r};t)$. Removing the time-dependencies again, we find an expression for the conjugate momentum which is consistent with the equations of motion:

$$\boldsymbol{\pi}(\mathbf{r}) = -i \sum_J \sqrt{\frac{\hbar\rho_{\mathrm{gr}}\omega_J}{2}} \left(b_J \bar{\mathbf{u}}_J(\mathbf{r}) - b_J^* \bar{\mathbf{u}}_J^*(\mathbf{r}) \right). \tag{2.63}$$

We now use the expansions in Eqs. (2.62) and (2.63) to express the expansion coefficients b_J and b_J^* in terms of $\mathbf{u}(\mathbf{r})$ and $\boldsymbol{\pi}(\mathbf{r})$ [42, 24, 43]. If we now quantize the fields $\mathbf{u}(\mathbf{r})$ and $\boldsymbol{\pi}(\mathbf{r})$, as well as the expansion coefficients, $b_J^{(*)} \rightarrow \hat{b}_J^{(\dagger)}$, we see that the canonical commutation relation implies that $[\hat{b}_J, \hat{b}_{J'}^\dagger] = \delta_{JJ'}$. These are the creation and annihilation operators of phonons of type J, which correspond to displacement fields $\bar{\mathbf{u}}_J(\mathbf{r})$. Using the expansions in Eqs. (2.62) and (2.63), the commutation relations of $\hat{b}_J^{(\dagger)}$, and Eq. (2.60), it can be shown that the Hamiltonian in Eq. (2.59) can be reduced to a sum over J of quantum harmonic oscillators with frequencies ω_J, which is a familiar result [1, 42].

The index J labels the solutions of Eq. (2.60). These solutions can be categorized into different vibrational modes, for which we introduce the index m. Within each mode m, the solutions can be further categorized by the wave vector $\mathbf{q}$. The Rayleigh waves described in subsection 2.2.2 constitute one such mode, $m = R$. Unlike other modes, it is localized in the y-direction with wave vector $\mathbf{q} = (q, 0)$ parallel to the edge. Rayleigh waves are thus labeled by the scalar q only [24]. A quantized acoustic field consisting only of the Rayleigh mode can then be written as the expansion

$$\hat{\mathbf{u}}_R(\mathbf{r}) = \int \frac{\mathrm{d}q}{2\pi}\sqrt{\frac{\hbar}{2\rho_{\mathrm{gr}}\omega_R(q)}}\left(\hat{b}_R(q)\bar{\mathbf{u}}_{R,q}(\mathbf{r}) + \hat{b}_R^\dagger(q)\bar{\mathbf{u}}_{R,q}^*(\mathbf{r})\right), \tag{2.64}$$

where $\bar{\mathbf{u}}_{R,q}(\mathbf{r})$ is given by Eq. (2.55) but must be normalized with respect to the inner product defined in Eq. (2.61). The operator $\hat{b}_R(q)$ ($\hat{b}_R^\dagger(q)$) is the annihilation (creation) operator for Rayleigh waves with wave vector q.

2.3 Electron-Strain Interaction

Strain in a graphene sheet causes deformations of the lattice which affect the electrons. The electron-strain interaction in graphene (presented below) was first calculated by Suzuura and Ando in 2001 when considering strain effects in carbon nanotubes [10].

The most straight-forward effect is that of hydrostatic deformation changing the size of the unit cell. The trace of the strain tensor, $u_{xx} + u_{yy}$, corresponds to a pure compression or dilation of the sheet, and thus of the individual unit cells. Changing the size of the unit cell changes the concentration of carriers, and thereby causes an energy shift. We model this effect by introducing a scalar potential proportional to the change in area due to deformation,

$$H^{(\tau)}_{\mathrm{int},AA} = H^{(\tau)}_{\mathrm{int},BB} = g_1(u_{xx} + u_{yy}). \tag{2.65}$$

The coupling constant has been estimated to $g_1 \approx 20$ eV [10]. The diagonal Hamiltonian matrix given by the above expression is invariant under the unitary transformaton defined by Eq. (2.12) and will be included in the full interaction Hamiltonian below.

In addition to changing the size of the unit cell, sheet deformations can also alter the shape of the lattice, such that the distance betwee nearest-neighbor atoms changes. This is usually modeled by assuming that the deformation simply changes the hopping energy between the atoms. In subsection 2.1.1 we assumed that the hopping energies to different nearest neighbors were equal, $t_1 = t_2 = t_3 \equiv t$. If we instead assume that the hopping energies between the nearest neighbors differ by a small amount, $t_n = t + \delta t_n$, $\delta t_n \ll t$, and neglect terms $\propto \delta t_n \mathbf{k}$ since both $|\mathbf{k}|$ and δt_n are assumed small[6],

---

[6] The fact that the interaction is an approximation to zeroth order in $\mathbf{k}$ means that, in this model, strain cannot change the Fermi velocity.

an additional term appears in the off-diagonal elements:

$$H^{(\tau)}_{\text{int},BA} = \frac{1}{2}\Big(\tau(\delta t_2 + \delta t_3 - 2\delta t_1) + i\sqrt{3}(\delta t_2 - \delta t_3)\Big)\,. \tag{2.66}$$

In the above, we have already included the effects of the unitary transformation defined by Eq. (2.12). In order to express the changes in hopping energy δt_n in terms of strain, we assume that

$$\delta t_n = -t\beta\frac{\boldsymbol{\delta R}_n \cdot (\mathbf{u}_{B,n} - \mathbf{u}_A)}{(a/\sqrt{3})^2}, \tag{2.67}$$

where $\mathbf{u}_A$ is the displacement of an A-atom and $\mathbf{u}_{B,n}$ is the displacement of its nearest-neighbor B-atom ($n = 1, 2, 3$). The hopping energy t and interatomic bond length $a/\sqrt{3}$ (a being the lattice constant) scales the energy and lengths, and $\beta \approx 2$ is a Grüneisen parameter [10]. In the theory of elasticity, we treat graphene as a continuous medium, not a discrete lattice, so we take the vector difference in Eq. (2.67) to the continuous limit and get

$$\mathbf{u}_{B,n} - \mathbf{u}_A \to \kappa(\boldsymbol{\delta R}_n \cdot \nabla)\mathbf{u}(\mathbf{r}), \tag{2.68}$$

where κ is a proportionality constant relating the discrete lattice to the continuous limit, and $\mathbf{u}(\mathbf{r})$ is the continuous 2D displacement field as defined in Eq. (2.40). The differentiations on the components of the displacement field lead to the introduction of the strain tensor as defined in subsection 2.2.1, and we arrive at

$$H^{(\tau)}_{\text{int},BA} = g_2\left(-\tau(u_{xx} - u_{yy}) + 2iu_{xy}\right), \tag{2.69}$$

where we defined the coupling constant

$$g_2 \equiv \hbar v_F\frac{\sqrt{3}\beta\kappa}{2a}\ , \tag{2.70}$$

which has been estimated to $g_2 \approx 2$ eV [10]. Comparing Eq. (2.69) with Eq. (2.13), we see that the strain interaction enters into the full electronic Hamiltonian similarily to a magnetic vector potential, $\mathbf{k} \to \mathbf{k} + \mathbf{A}^{(\tau)}$. For this reason, the interaction elements given by Eq. (2.69) are sometimes referred to as a *strain-induced pseudomagnetic field* [44]. However, unlike a real magnetic field, strain does not break time-reversal symmetry[7].

---

[7] Since the wave vectors of the K- and K'-points are related by a sign reversal, the two valleys are related by time reversal [13]. The preservation of time-reversal symmetry is guaranteed by the interplay of the τ in Eq. (2.69) and those in Eq. (2.13).

We now include both the off-diagonal "pseudomagnetic field" of Eq. (2.69) and the scalar deformation potential of Eq. (2.65) in an electron-strain interaction Hamiltonian which we write using sublattice-space Pauli matrices as

$$\boldsymbol{H}_{\text{int}}^{(\tau)}\left[\mathbf{u}(x,y;t)\right] = g_1(u_{xx}+u_{yy})\boldsymbol{I} + g_2(-\tau(u_{xx}-u_{yy})\boldsymbol{\sigma}_x + 2u_{xy}\boldsymbol{\sigma}_y). \quad (2.71)$$

Here, we have explicitly written the dependence of the interaction Hamiltonian on the displacement field $\mathbf{u}(x,y;t)$. In the case of a quantized acoustic field, the strain-tensor components are operators, $u_{ij} \rightarrow \hat{u}_{ij}$, defined in terms of their associated displacement-field operator $\hat{\mathbf{u}}(x,y;t)$.

Chapter 3

Results & Discussion

In this chapter we summarize and discuss the appended papers, and also clarify certain points, e.g., the derivation of the 1D Hamiltonian in paper II. In both papers, we consider a zigzag edge of a graphene sheet in a perpendicular magnetic field and investigate the interaction between mechanical Rayleigh edge waves and electronic edge states, as modeled in Chapter 2.

3.1 Resonant Interaction

A gate voltage is applied to the graphene sheet so that at least two electronic bands of edge states cross the chemical potential (see Fig. 2.6). We then consider the interaction between an acoustic field of Rayleigh waves and the electronic subsystem. We will initially model the acoustic field as purely classical. We will investigate how interaction with the acoustic field couples electronic states, and show that resonant interaction can occur between different bands, at points near the chemical potential.

In the presence of the acoustic field, the interaction between it and the electronic subsystem causes the the electronic edge states to no longer be true eigenstates of the Hamiltonian. Thereby the electronic edge states are coupled to each other by the interaction. Since the acoustic field is smooth on the scale of the lattice spacing, $q \ll |\mathbf{K}-\mathbf{K}'| \sim a^{-1}$, it cannot mix valleys, so we only need to consider intravalley coupling. The electronic state i (f) can be specified by the valley index τ, the wave vector $\tilde{k}_i$ ($\tilde{k}_f$) and the band indices n_i (n_f) and $\varkappa_i$ ($\varkappa_f$). The energy of a state is then given by $\tilde{E}_i(\tilde{k}_i)$ as shown in Fig. 2.6, where i represents the set of indices $\{\tau, n_i, \varkappa_i\}$ (and analogously for f). The matrix element[1] coupling the states i and f is given by

$$
\begin{aligned}
&\langle f|\, \hat{H}^{(\tau)}_{\text{int}}\, [\bar{\mathbf{u}}_{R,q}(\mathbf{r};t)]\, |i\rangle = \\
&= l_B^2 \iint \mathrm{d}\tilde{x}\, \mathrm{d}\tilde{y}\, \boldsymbol{\psi}^{\dagger}_{\tilde{k}_f,f}(\tilde{x},\tilde{y}) \boldsymbol{H}^{(\tau)}_{\text{int}}\, [\mathbf{u}_{R,q}(\tilde{x}l_B,\tilde{y}l_B;t)]\, \boldsymbol{\psi}_{\tilde{k}_i,i}(\tilde{x},\tilde{y}) e^{iE_B\Delta\tilde{E}t/\hbar}, \quad (3.1)
\end{aligned}
$$

where $\nu_j = \tilde{E}_j^2(\tilde{k}_j)$ ($j = i, f$), and $\Delta\tilde{E} \equiv \tilde{E}_f(\tilde{k}_f) - \tilde{E}_i(\tilde{k}_i)$. The interaction Hamiltonan $\boldsymbol{H}^{(\tau)}_{\text{int}}$ is given by Eq. (2.71), and the acoustic field $\mathbf{u}_{R,q}(x,y;t)$ which enters into it is given by Eq. (2.58). The electronic pseudospinors are given by Eqs. (2.35), (2.36), (2.37), and (2.38). Carrying out the $\tilde{x}$-integration and rewriting, we get

$$
\begin{aligned}
\langle f|\, \hat{H}^{(\tau)}_{\text{int}}\, [\bar{\mathbf{u}}_{R,q}(\mathbf{r};t)]\, |i\rangle &= 2\pi l_B \delta(\tilde{k}_f - \tilde{k}_i - \tilde{q}) V_{fi}(\tilde{q}) e^{iE_B(\Delta\tilde{E} - \tilde{s}_R|\tilde{q}|)t/\hbar} + \\
&+ 2\pi l_B \delta(\tilde{k}_f - \tilde{k}_i + \tilde{q}) V_{fi}(-\tilde{q}) e^{iE_B(\Delta\tilde{E} + \tilde{s}_R|\tilde{q}|)t/\hbar}, \quad (3.2)
\end{aligned}
$$

where the scaled speed of sound is $\tilde{s}_R \equiv s_R/(\sqrt{2}v_F)$, and

$$
V_{fi}(\tilde{q}) = \frac{i\tilde{q}}{l_B} u_0 (F_1 g_1 + F_2 g_2). \quad (3.3)
$$

The quantities F_1 and F_2 (which have had their indices suppressed for brevity) contain the nondimensionalized $\tilde{y}$-integrals of the interaction terms proportional to the coupling constants g_1 and g_2, respectively. We will refrain from giving the explicit expression for these quantities here; they can be found in the appendix to paper I.

From Eq. (3.2) it is clear that the interaction is strongest when $\tilde{q} = \pm(\tilde{k}_f - \tilde{k}_i)$ and simultaneously $\Delta\tilde{E} = \pm\tilde{s}_R|\tilde{q}|$, i.e. when the acoustic field is at a resonance with two electronic states f and i. The two terms in Eq. (3.2) then correspond to two different possible resonances, one where $\Delta\tilde{E} > 0$ and one where $\Delta\tilde{E} < 0$. Because the speed of sound $\tilde{s}_R$ is much smaller than the typical electronic velocities, it can be shown that energy and momentum conservation causes intraband matrix elements to vanish. The exception to this is the case in which one of the states is an edge state and the other is at large negative $\tilde{k}$, essentially a bulk state. In this case the matrix element will

---

[1] In paper I, we used the notation $\Lambda^{\tau}_{\tilde{k}_f,\tilde{k}_i}$ for this matrix element and explicitly extracted the momentum conserving factor.

vanish due to the different regions of localization. Thus we may conclude that it is sufficient to consider interband coupling, $n_i \neq n_f$.

We note that we must have that the initial (final) state i (f) is occupied (unoccupied). At equilibrium, this corresponds to the initial (final) state lying below (above) the chemical potential. Since the speed of sound is much smaller than the electronic velocities, it follows that resonances can occur only in a narrow region of energies near the chemical potential. This conclusion is still valid for the case when the electrons are initially at equilibrium but are allowed to build up a nonequilibrium through interaction with the acoustic field, since states far from the chemical potential are out of reach of the interaction and thus remain at equilibrium. It follows that resonant coupling occurs only between the bands that cross the chemical potential.

At equilibrium, unoccupied states have higher energies than occupied states, so resonances where $\Delta\tilde{E} < 0$ can be neglected. In what follows, we will only consider the first ($\Delta\tilde{E} > 0$ resonance) term in Eq. (3.2). The condition for resonance between a pair of electronic states at $\tilde{k}_{i,r}$ and $\tilde{k}_{f,r}$ (index r for "resonance") and the acoustic field with wave vector q is

$$\begin{aligned} \tilde{q} &= \tilde{k}_{f,r} - \tilde{k}_{i,r} \equiv \Delta\tilde{k}, \\ \tilde{s}_R|\Delta\tilde{k}| &= \tilde{E}_f(\tilde{k}_{f,r}) - \tilde{E}_i(\tilde{k}_{i,r}). \end{aligned} \tag{3.4}$$

We will now assume that this condition is fulfilled for some states at $\tilde{k}_{i,r}$ and $\tilde{k}_{f,r}$, and write

$$\tilde{k}_j = \tilde{k}_{j,r} + \delta\tilde{k}_j, \quad \delta\tilde{k}_j \ll 1, \quad j = i, f, \tag{3.5}$$

i.e. we are considering near-resonant states. We may now linearize the electronic spectrum around the resonant states so that

$$\begin{aligned} \tilde{E}_j(\tilde{k}_j) &\approx \tilde{E}_j(\tilde{k}_{j,r}) + \delta\tilde{E}_j(\delta\tilde{k}_j), \\ \delta\tilde{E}_j(\delta\tilde{k}_j) &= \tilde{v}_j\delta\tilde{k}_j, \quad j = i, f. \end{aligned} \tag{3.6}$$

The dimensionless electronic velocity appearing in the linearization is $\tilde{v}_j = v_j/(\sqrt{2}v_F)$ (cf. $\tilde{s}_R$ above), where v_j is the physical velocity at the corresponding point in the unscaled spectrum. As an approximation, we may evaluate the integrals F_1 and F_2 in $V_{fi}(\Delta\tilde{k})$ only at the resonant states (as defined by Eq. 3.4). Then $V_{fi}(\Delta\tilde{k})$ is just an energy which is specific to each resonance.

Since only states near the chemical potential are involved in the process, it follows that the resonant electronic wave vector $\tilde{k}_{i,r}$ ($\tilde{k}_{f,r}$) can be approximated by the wave vector where the band n_i (n_f) crosses the chemical potential, which we define to be $\tilde{k}_{F,i}$ ($\tilde{k}_{F,f}$), and the energies as $\tilde{E}_i \approx \tilde{E}_f \approx \tilde{\mu}$.

($\tilde{\mu} \equiv \mu/E_B$.) As a further approximation, we can also perform the linearization of the spectrum at the chemical potential, and take the resonant acoustic wave vector to be $\Delta\tilde{k} \approx \Delta\tilde{k}_F$, where $\Delta\tilde{k}_F \equiv \tilde{k}_{F,f} - \tilde{k}_{F,i}$ is the wave vector separation of the bands n_f and n_i at the chemical potential[2].

3.2 Weak Perturbation (Paper I)

We investigate the case when the acoustic field has a low enough amplitude that the system dynamics are well described by first order perturbation theory during the time before the electronic system relaxes to equilibrium. For these small vibrational amplitudes, we find that the coupling between resonant electronic states can cause an attenuation of the acoustic field.

We consider a resonance of the type described in Section 3.1 and introduce a finite electronic relaxation time τ_{el} (due to e.g., edge defects, impurities); then the electronic subsystem will only evolve dynamically for a time on the order of τ_{el} before it relaxes to equilibrium. Therefore, if the vibrational amplitude u_0 is small enough that $V_{fi} \propto u_0$ fulfills

$$|V_{fi}(\Delta\tilde{k})| \ll \frac{\hbar}{\tau_{\mathrm{el}}}, \tag{3.7}$$

then we may use linear perturbation theory. Specifically, we will use *Fermi's golden rule* to get the probability of transition per unit time —the "transition rate" —from a specific (resonant) initial state i to *a continuum* of final states f (all near-resonance states in the band n_f) via interaction with the acoustic field. This is given by

$$W_{fi} = \frac{2\pi}{\hbar}|V_{fi}(\Delta\tilde{k})|^2 \rho_f(E_f) \tag{3.8}$$

where $\rho_f(E_f)$ is the density of final states, and transitions must respect conservation of energy [45]. We can represent the energy conservation by introducing an integration over final energies $\delta E_f = \delta\tilde{E}_f E_B$, and a delta function. If we linearize the spectrum of near-resonance states f as described in Section 3.1, we get the density of final states per unit length (note that this is

---

[2] In paper I, we never made a distinction between the resonant states and the states at the chemical potential. The difference is negligible when considering the transition rate, but is made here for the sake of completeness.

written using unscaled quantities):

$$\rho_f(E_f) = \frac{1}{2\pi\hbar|v_f|}. \tag{3.9}$$

We now consider the transition rate from *all* near-resonance initial states i to all near-resonance states f (for $\Delta\tilde{E} > 0$). We introduce a $\delta\tilde{k}_i$-integration over initial states and keep the momentum-conserving delta function in Eq. (3.2). We get the transition rate per unit length,

$$W = \iint \mathrm{d}\delta\tilde{k}_i \, \mathrm{d}\delta\tilde{E}_f \, \delta((\delta\tilde{E}_f/\tilde{v}_f) - \delta\tilde{k}_i) W_{fi} \delta(\delta\tilde{E}_f - \tilde{v}_i\delta\tilde{k}_i). \tag{3.10}$$

It is here assumed that all initial (final) states lie below (above) the chemical potential[3].

We combine Eqs. (3.10), (3.9) and (3.8) and carry out the integrations using the delta functions. We find

$$W = \frac{|V_{fi}(\Delta\tilde{k})|^2}{\hbar^2|v_f - v_i|}. \tag{3.11}$$

The matrix element $V_{fi}(\Delta\tilde{k})$ is given by Eq. (3.3), and may be evaluated at the chemical potential.

Eq. (3.11) describes the transition rate per unit length between two resonant electronic populations in different bands. The energy for each such transition, $E_B\Delta\tilde{E} = \hbar\omega_R(\Delta k) > 0$ ($\Delta k = \Delta\tilde{k}/l_B$), is taken from the acoustic field, thus causing it to attenuate. The total energy of the acoustic field is given by $E_{\mathrm{ac}} = \rho_{\mathrm{gr}}\omega_R^2(\Delta k)\langle \mathbf{u}_{R,q}, \mathbf{u}_{R,q}\rangle$, where the inner product is just the position integral, as defined in Eq. (2.61) [24]. If we multiply the transition rate by the proportion of energy lost in each transition, $\hbar\omega_R(\Delta k)/E_{\mathrm{ac}}$, we get an expression for the decay rate of acoustic energy,

$$\Gamma = \frac{|N_{\mathrm{ac}}|^2|\Delta k|^2|F_1 g_1 + F_2 g_2|^2}{2\hbar|v_f - v_i|\rho_{\mathrm{gr}} s_R}, \tag{3.12}$$

where N_{ac} is

$$N_{\mathrm{ac}} = \left(\int_0^\infty \mathbf{f}_q^*(y) \cdot \mathbf{f}_q(y) \, \mathrm{d}(|q|y)\right)^{-1/2} \approx 1.2, \tag{3.13}$$

---

[3] If this was not the case, we would have to include a factor $f_F(E_i)(1 - f_F(E_f))$ in the integrand, where $f_F(E)$ is the Fermi distribution function. With the given assumption, this factor is approximately equal to one (assuming low temperature).

independent of q (see Eq. (2.56))[4]. Instead of the decay rate Γ, we can use its reciprocal, the decay time $\tau_D = 1/\Gamma$. In terms of the decay time, the energy of the acoustic field decays as $\sim \exp(-t/\tau_D)$.

As an example, we consider the case when the chemical potential is positioned precisely in the middle of the gap between bulk Landau levels 1 and 2, and consider the transition rate from energy band $n_i = 1$ to $n_f = 0$ (the wave functions in Fig. 2.5 correspond to these states). At equilibrium, this is the only possible resonance due to the "missing" band in the K'-spectrum (see Section 2.1.3). We find $F_1 g_1 + F_2 g_2 \approx -1.3$ eV. The electronic velocites v_i can be estimated from the slope of the energy bands in the spectrum (Fig. 2.6). We then get an acoustic decay time $\tau_D \approx 3.4$ ns$/B[T]$. It should be noted that these calculations did not include a factor 2 for the spin degeneracy. Inclusion of this factor would halve the decay time.

We then consider the case when the gate voltage and the frequency of the acoustic field is kept fixed but the magnetic field B is modulated, and calculate Γ as a function of magnetic field numerically. Changing the magnetic field alters the separation energy E_B (E_1 in paper I) between bulk Landau levels, causing the levels to change position with respect to the chemical potential as long as there is a finite gate voltage. E.g., decreasing B causes the energy levels to drop below the chemical potential, thus increasing the number of energy bands crossing it. This effect becomes simplified when considering the scaled energy spectrum (Fig. 2.6). Since the shape of the scaled spectrum is independent of the magnetic field, the only effect is a change in the position of the (scaled) chemical potential $\tilde{\mu} = \mu/E_B \propto 1/\sqrt{B}$.

We gradually reduce B, causing the chemical potential $\tilde{\mu}$ to rise through the scaled spectrum. For each value of B, we then rescale the acoustic wave vector, $\tilde{q} = q l_B$, and calculate Γ due to any and all transitions between the electronic bands. We do this for both the K- and K'-valley spectra and plot the result against $1/\sqrt{B[T]}$. In addition, for each included transition, we plot a line in the spectrum between the resonant states, with the line opacity proportional to Γ. The lines in the spectrum, from lowest energy to highest, then correspond to the absorption peaks from lower to higher $1/\sqrt{B[T]}$. We can thus easily identify the contribution from each transition to the absorption of acoustic energy. The plots are presented in paper I, Figs. 4 and 5. In this numerical calculation, we introduced a small, finite

---

[4] This is actually the material-parameter part of the normalization constant of $\bar{\mathbf{u}}_{R,q}$, which is $N_{\mathrm{ac}}\sqrt{|q|}$ (see Subsection 2.2.3).

temperature and linearized the spectrum around the resonant states instead of at the chemical potential (this is more accurate, but the difference is negligible). We did not include the factor 2 for spin degeneracy.

3.3 Nonlinear Regime (Paper II)

We now consider acoustic amplitudes large enough that the linear theory (e.g., Fermi's golden rule) breaks down, i.e. Eq. (3.7) is no longer true. We then consider the full nonlinear system of equations describing the resonant coupling between the electronic and acoustic subsystems. We solve the system self-consistently, and find that it admits solutions where the acoustic field consists of a hypersonic soliton. In contrast to paper I, we start with a *quantized* acoustic field of Rayleigh edge waves (see Subsection 2.2.3). Note that we will not be using scaled quantities in this section[5].

For simplicity, we consider the case when the chemical potential is positioned in the middle of the gap between bulk Landau levels 1 and 2. There are then two electronic bands intersecting the chemical potential in the K-valley, and only one in the K'-valley. Since the acoustic field cannot mix valleys, we only need to consider the resonant coupling between the two bands in the K-valley. We linearize the spectrum near the chemical potential (as described in Section 3.1) and reduce our 2D system to an effective 1D model for the edge by taking the y-dependent parts of electronic wave functions as equal for all states in the same resonant population, i.e. we neglect their k-dependence (these functions of y are those depicted in Fig. 2.5).

As an example of this 2D → 1D method, let us consider the acoustic subsystem. We begin by considering the quantized acoustic field given in Eq. (2.64). If the wave vectors of the acoustic field are concentrated at the resonant wave vectors, $q \approx \pm\Delta k \approx \pm\Delta k_F$, we may split the q-integral into two δq-integrals —one where $q = \Delta k_F + \delta q$, and one where $q = -\Delta k_F + \delta q$. As an approximation, we then take $\omega_R(q) \approx \omega_R(\Delta k_F)$ in the square root of the prefactor, and $\mathbf{f}_q(y) \approx \mathbf{f}_{\pm\Delta k_F}(y)$. The phononic creation and annihilation operators now describe two different kinds of phonons, so we introduce a new pair of commuting phononic operators: $\hat{b}_R(\pm\Delta k_F + \delta q) \equiv \hat{b}_\pm(\delta q)$. If we now

---

[5] And note especially that while $\tilde{v}$ in paper I represented a nondimensionalized velocity, in the notation of paper II it would instead represent v in a moving reference frame.

exploit the fact that $\mathbf{f}^*_{\Delta k_F}(y) = \mathbf{f}_{-\Delta k_F}(y)$, we may reorder terms so that

$$\hat{\mathbf{u}}_R(\mathbf{r}) = \sqrt{\frac{\hbar}{2\rho_{\mathrm{gr}}\omega_R(\Delta k_F)}} \Big[\mathbf{f}_{\Delta k_F}(y)e^{i\Delta k_F x}\left(\hat{u}_+(x) + \hat{u}^\dagger_-(x)\right) + \\ +\mathbf{f}^*_{\Delta k_F}(y)e^{-i\Delta k_F x}\left(\hat{u}^\dagger_+(x) + \hat{u}_-(x)\right)\Big], \quad (3.14)$$

where

$$\hat{u}_\pm(x) = \int \frac{d\delta q}{2\pi} e^{i\delta q x}\hat{b}_\pm(\delta q). \quad (3.15)$$

These 1D operators fulfill the commutation relation

$$\left[\hat{u}_\pm(x), \hat{u}^\dagger_\pm(x')\right] = \delta(x - x'); \quad (3.16)$$

all nonequivalent commutators being zero. As mentioned in Subsection 2.2.3, the full acoustic Hamiltonian in Eq. (2.59) can be written as a summation of harmonic oscillators, one for each mode and wave vector. For a field of Rayleigh waves, we get (up to an additive constant energy)

$$\hat{H}_{\mathrm{ac}} = \int \frac{\mathrm{d}q}{2\pi}\hbar\omega_R(q)\hat{b}^\dagger_R(q)\hat{b}_R(q), \quad (3.17)$$

where the number of Rayleigh-mode phonons are counted by the number operator $\hat{b}^\dagger_R(q)\hat{b}_R(q)$ for each wave vector q. We split this integral in the same way as in the derivation of Eq. (3.14), and get

$$\hat{H}_{\mathrm{ac}} = \int \frac{\mathrm{d}\delta q}{2\pi}\hbar s_R(\Delta k_F + \delta q)\hat{b}^\dagger_+(\delta q)\hat{b}_+(\delta q) + \\ + \int \frac{\mathrm{d}\delta q}{2\pi}\hbar s_R(\Delta k_F - \delta q)\hat{b}^\dagger_-(\delta q)\hat{b}_-(\delta q), \quad (3.18)$$

and then use Eq. (3.15) to write this in terms of the operators $\hat{u}_\pm(x)$. Replacing δq with derivatives $\pm i\partial_x$, we get

$$\hat{H}_{\mathrm{ac}} = \int \hbar s_R \hat{u}^\dagger_+(x)(\Delta k_F - i\partial_x)\hat{u}_+(x)\,\mathrm{d}x + \\ + \int \hbar s_R \hat{u}^\dagger_-(x)(\Delta k_F + i\partial_x)\hat{u}_-(x)\,\mathrm{d}x\,, \quad (3.19)$$

which is a 1D Hamiltonian with position-space operators. The electronic subsystem and the interaction Hamiltonian can be reduced to 1D in a similar way (see paper II). A constant, Λ, then appears in the 1D interaction Hamiltonian[6]; it is related to the acoustic decay rate Γ (Eq. (3.12)) of this resonance as $\Lambda^2 = |v_0 - v_1|\Gamma$. We then proceed to derive and solve the equations of motion for this 1D system.

At one point, we replace the quantized acoustic field $\hat{u}_+$ with a classical field. The motivation for this is that a large amplitude corresponds to a huge number of phonons. In this case, acting on the state with an operator $\hat{b}^{(\dagger)}$ to add or subtract *one* phonon has a negligible effect on the state, but the factor which emerges when the operator acts on the state is huge, since it is proportional to the square root of the number of phonons. We may therefore replace the operator with this number, thereby neglecting its effect on the state.

Eventually, we arrive at a family of self-consistent solutions for the full set of equations. The acoustic field in this type of solution is a traveling hyperbolic secant profile modulated by the resonance frequency,

$$\begin{aligned}\mathbf{u}_T(\mathbf{r};t) = {} & \frac{\lambda}{2\pi^2}\left(\frac{\hbar v_{\text{eff}}\Delta k_F}{g_R}\right)\left(\frac{\lambda}{L}\right)\operatorname{sech}\left(\frac{x-vt}{L}\right)\cdot \\ & \cdot\begin{pmatrix}(e^{-\lambda_l|\Delta k_F|y} - C_x e^{-\lambda_t|\Delta k_F|y})\cos\left(\Delta k_F x - \omega_r t\right) \\ (-\lambda_l e^{-\lambda_l|\Delta k_F|y} + C_y e^{-\lambda_t|\Delta k_F|y})\sin\left(\Delta k_F x - \omega_r t\right)\end{pmatrix},\end{aligned} \tag{3.20}$$

where $v_{\text{eff}} = \sqrt{(v_0 - v)(v_1 - v)}$, $g_R = |F_1 g_1 + F_2 g_2| \approx 1.3$ eV, λ is the acoustic wave length, $\omega_r = s_R|\Delta k|$, $L = T \cdot v$, and the soliton velocity v is given by

$$v = \frac{s_R}{1 - \frac{1}{2}\Gamma T}. \tag{3.21}$$

A parameter T, which we interpret as the duration of an acoustic pulse, couples the velocity, amplitude and width of the profile, and we find that increasing the amplitude reduces the velocity, and vice versa (see Fig. 3.1). It is found that the speed of these solitons can significantly exceed that of regular Rayleigh edge waves. For the solitons to exists, the pulse duration T must satisfy

$$\frac{1}{\tau_{\text{el}}} \ll \frac{1}{T} \ll \omega_r. \tag{3.22}$$

---

[6] Not the same as the quantity $\Lambda^{\tau}_{\tilde{k}_f,\tilde{k}_i}$ in paper I.

Also, we must have that $T < 2/\Gamma$ so that Eq. (3.21) does not diverge. Another restriction is that T must be such that the soliton velocity is less than the electronic velocities, $v < v_1, v_0$, otherwise v_{eff} becomes imaginary. However, this restriction only amounts to a small correction to the one already mentioned: $T < 2/\Gamma(1 - (s_R/v_1))$ (since $v_1 < v_0$).

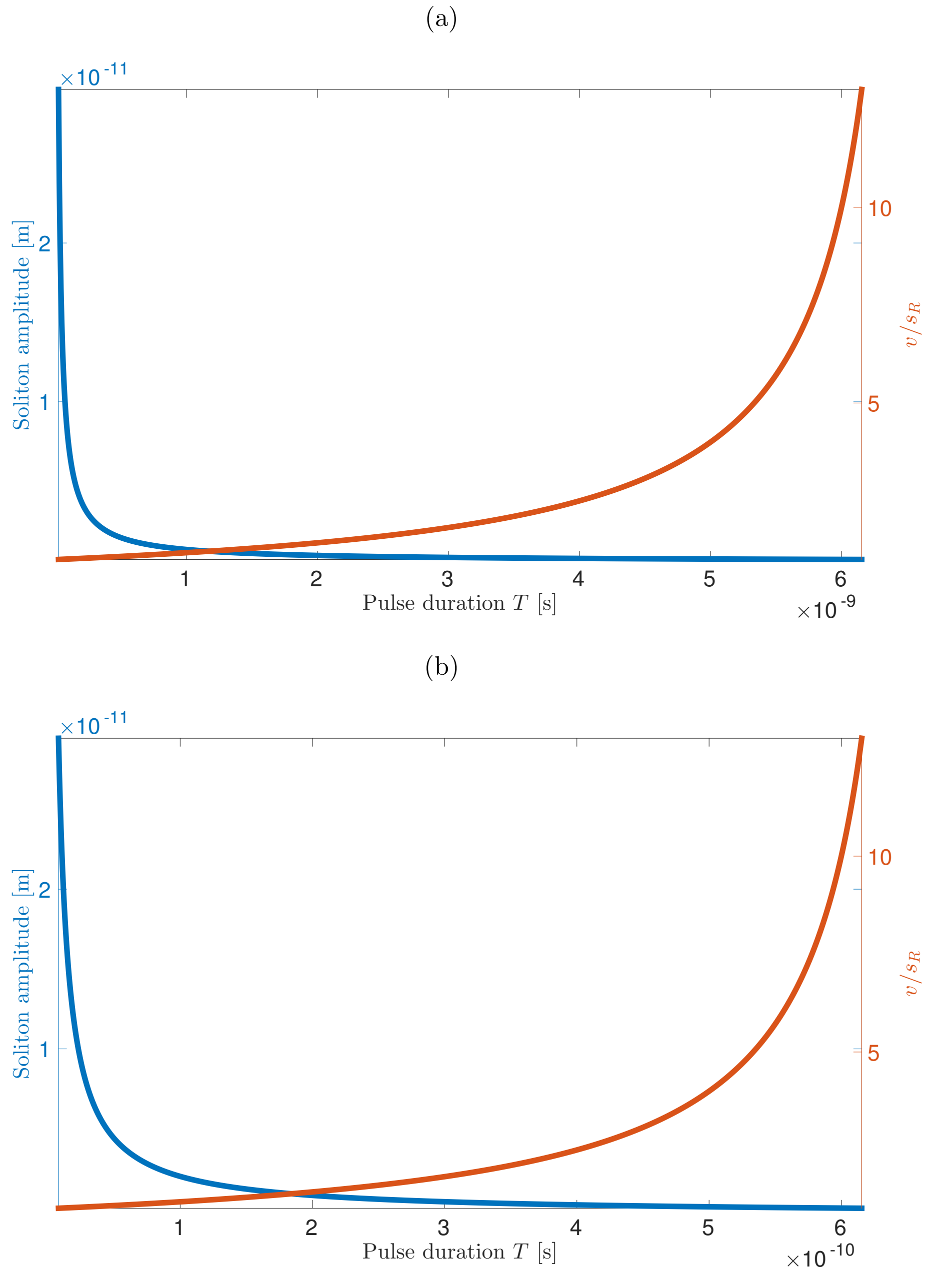

Figure 3.1: The soliton amplitude (blue) and scaled velocity v/s_R (red) plotted against the pulse duration T for $B = 1$ T and $\omega_r = 7.9 \cdot 10^{11}$ s^{-1} **(a)** and $B = 10$ T and $\omega_r = 2.5 \cdot 10^{12}$ s^{-1} **(b)**.

Chapter 4

Summary & Outlook

4.1 Summary

The aim of this thesis was to investigate the interaction between in-plane vibrational edge modes and electronic edge states in a sheet of graphene in a perpendicular magnetic field. The edge was taken to be zigzag and the magnetic field was strong enough compared to the temperature to cause formation of distinct electronic energy bands.

Depending on the gate voltage, several energy bands can cross the chemical potential. If the acoustic field contains wave vectors that roughly match the k-space separation of the points where the electronic bands cross the chemical potential, then the acoustic field can resonantly interact with the electrons. States far from the chemical potential are inert due to the smallness of the speed of sound compared to typical electron velocities. For low-amplitude acoustic waves, the resonant interaction causes an attenuation of the waves [46]. For higher vibrational amplitudes, when nonlinear effects become important, the acoustic field can interact with the electrons in such a way as to produce acoustic solitons, moving with speeds higher than the regular speed of sound. The amplitude, velocity and width of such solitons are coupled. E.g., an increase in the velocity is accompanied by a decrease in the amplitude.

4.2 Outlook

4.2.1 Time-of-flight Experiment

If the modeled system would be realized experimentally, with the possibility to both generate and detect mechanical edge waves, then it should be possible to test both of the described effects (attenuation and soliton formation) in a time-of-flight experiment. The theory predicts that the propagation of low-amplitude acoustic waves is blocked[1] for certain combinations of magnetic field strength, gate voltage, and acoustic frequency. Therefore, varying these parameters and measuring whether an acoustic pulse makes it to the detector or not would corroborate or invalidate the theory. Since the acoustic edge waves have an essentially 1D wave front, they do not attenuate during propagation in the absence of defects [47, 41]. This could potentially make the blocking effect more prominent, and thus easier to detect. The theory further predicts that if the vibrational amplitude is increased, then acoustic soliton formation is possible. These solitons should appear for the same conditions as those for which the propagation was blocked (i.e. when there is a resonant interaction). These solitons can achieve velocities significantly higher than the speed of sound. Therefore, they could be detected by measuring the time it takes for an acoustic pulse to reach the detector. This also helps distinguish these solitons from any acoustic solitons that may have formed due to inherent nonlinearities in the sheet mechanics [48]. Varying the length of acoustic pulses could test the predicted relationship between pulse duration, soliton amplitude and velocity.

4.2.2 Electronic Relaxation Mechanism

In the experiment described above, acoustic pulses are generated intentionally, interacts with the electronic subsystem, and are then detected. It is possible to conceive of the reverse situation. If one realized the system in which the chemical potential is different for two electronic bands, the system would seek to restore equilibrium by moving electrons from one band to the other. Interaction with the acoustic subsystem could be one way in which this could occur. Then the electronic subsystem could give rise to mechanical Rayleigh edge waves, and possibly even hypersonic solitons. Then the

---

[1] If the time during which the waves propagate from their source to the detector is large enough for them to have significantly attenuated.

solitons would essentially be a mechanism for relaxation of the electronic subsystem.

4.2.3 Sensor Applications

The Rayleigh edge waves themselves, without considering any interaction with electrons, could have potential sensor applications. Surface acoustic waves are widely used to detect surface adsorbants. This is done by measuring the decay and velocity shift of the waves induced by the extra material on the surface [49, 50, 51, 52]. In a graphene sheet, the only dangling bonds to which an atom or molecule could attach are those at the edges. It is possible that the presence of alien atoms or molecules on the edge could induce a decay and/or a velocity shift in the edge waves, in a way analogous to the surface wave case, thereby allowing for detection of the attached mass.

4.2.4 Additional Theoretical Work

The arguably most obvious improvement upon the theory would be to include flexural motion as well, since it is known that there are also flexural edge vibrations [48]. Another possible improvement would be to consider multi-soliton solutions as well. Such solutions are expected from comparison with similar systems [53].

During the work on paper II, there was an attempt to treat the system with the bosonization technique from 1D quantum theory. This attempt ultimately led nowhere, and bosonization was soon abandoned in favor of other methods. But it is well-known that the electronic edge states can be treated using this theory [42], and the attempt initially seemed promising. For these reasons, revisiting the bosonization technique could be a possible continuation of the work in this thesis.

ACKNOWLEDGMENTS

I would like to thank my supervisor, Leonid Gorelik, without whom this thesis would not exist, my colleagues, who make work something to look forward to, and all my close friends and family members, who make it all worth it.

Bibliography

[1] Ashcroft and Mermin. *Solid State Physics*. Brooks/Cole, 1976.

[2] H.W. Kroto, J.R. Heath, S.C. O'Brien, R.F. Curl, and R.E. Smalley. C60: Buckminsterfullerene. *Nature*, 318:162–163, 1985.

[3] O.A. Shenderova, V.V. Zhirnov, and D.W. Brenner. Carbon nanostructures. *Critical Reviews in Solid State and Materials Sciences*, 27(1–4):227–356, 2002.

[4] L. Radushkevich and V.M. Lukyanovich. *Journal of physical chemistry*, 26:88–95, 1952.

[5] Sumio IIjima. Helical microtubules of graphitic carbon. *Nature*, 354:56–58, 1991.

[6] M.S. Dresselhaus and G. Dresselhaus. Intercalation compounds of graphite. *Advances in Physics*, 51(1):1–186, 2002.

[7] P. R. Wallace. The band theory of graphite. *Phys. Rev.*, 71:622–634, May 1947.

[8] G. Dresselhaus and M. S. Dresselhaus. Spin-orbit interaction in graphite. *Phys. Rev.*, 140:A401–A412, Oct 1965.

[9] Riichiro Saito, Gene Dresselhaus, Mildred S Dresselhaus, et al. *Physical properties of carbon nanotubes*, volume 35. World Scientific, 1998.

[10] Hidekatsu Suzuura and Tsuneya Ando. Phonons and electron-phonon scattering in carbon nanotubes. *Phys. Rev. B*, 65:235412, May 2002.

[11] K. S. Novoselov, A. K. Geim, S. V. Morozov, D. Jiang, Y. Zhang, S. V. Dubonos, I. V. Grigorieva, and A. A. Firsov. Electric field effect in atomically thin carbon films. *Science*, 306(5696):666–669, 2004.

[12] L. D. Landau and E. M. Lifshitz. *Statistical Physics, Part I.* Butterworth-Heinemann, Oxford, 2011.

[13] A. H. Castro Neto, F. Guinea, N. M. R. Peres, K. S. Novoselov, and A. K. Geim. The electronic properties of graphene. *Rev. Mod. Phys.*, 81:109–162, Jan 2009.

[14] K. S. Novoselov, A. K. Geim, S. V. Morozov, D. Jiang, M. I. Katsnelson, I. V. Grigorieva, and S. V. Dubonos. Two-dimensional gas of massless dirac fermions in graphene. *Nature*, 438:197, November 2005.

[15] K.I. Bolotin, K.J. Sikes, Z. Jiang, M. Klima, G. Fudenberg, J. Hone, P. Kim, and H.L. Stormer. Ultrahigh electron mobility in suspended graphene. *Solid State Communications*, 146(9–10):351 – 355, 2008.

[16] Changgu Lee, Xiaoding Wei, Jeffrey W. Kysar, and James Hone. Measurement of the elastic properties and intrinsic strength of monolayer graphene. *Science*, 321(5887):385–388, 2008.

[17] The Royal Swedish Academy of Sciences. Scientific background on the nobel prize in physics 2010. October 2010.

[18] Thomas C. Hales. The honeycomb conjecture. *Discr. Comput. Geom.*, 25:1–22, 2001.

[19] Vikas Berry. Impermeability of graphene and its applications. *Carbon*, 62:1 – 10, 2013.

[20] R. R. Nair, P. Blake, A. N. Grigorenko, K. S. Novoselov, T. J. Booth, T. Stauber, N. M. R. Peres, and A. K. Geim. Fine structure constant defines visual transparency of graphene. *Science*, 320(5881):1308, 2008.

[21] J Wang, M Liang, Y Fang, T Qiu, J Zhang, and L Zhi. Rod-coating: towards large-area fabrication of uniform reduced graphene oxide films for flexible touch screens. *Advanced materials (Deerfield Beach, Fla.)*, 24(21):2874–2878, 2012.

[22] A. K. Geim and K. S. Novoselov. The rise of graphene. *Nat. mater.*, 6:183–191, March 2007.

[23] L. D. Landau and E. M. Lifshitz. *Theory of Elasticity.* Butterworth-Heinemann, Oxford, 2008.

[24] Hiroshi Ezawa. Phonons in a half space. *Ann. Phys.*, 67:438–460, 1971.

[25] F. Mandl and G. Shaw. *Quantum Field Theory.* John Wiley & Sons, Chichester, 2008.

[26] Daniel R. Cooper, Benjamin DAnjou, Nageswara Ghattamaneni, Benjamin Harack, Michael Hilke, Alexandre Horth, Norberto Majlis, Mathieu Massicotte, Leron Vandsburger, Eric Whiteway, and Victor Yu. Experimental review of graphene. *ISRN Condensed Matter Physics*, 2012:56, 2012.

[27] Igor Romanovsky, Constantine Yannouleas, and Uzi Landman. Unique nature of the lowest landau level in finite graphene samples with zigzag edges: Dirac electrons with mixed bulk-edge character. *Phys. Rev. B*, 83:045421, Jan 2011.

[28] L. Brey and H. A. Fertig. Electronic states of graphene nanoribbons studied with the dirac equation. *Phys. Rev. B*, 73:235411, Jun 2006.

[29] V. P. Gusynin, V. A. Miransky, S. G. Sharapov, and I. A. Shovkovy. Edge states in quantum hall effect in graphene (review article). *Low Temperature Physics*, 34(10):778–789, 2008.

[30] Luis Brey and H. A. Fertig. Edge states and the quantized hall effect in graphene. *Phys. Rev. B*, 73:195408, May 2006.

[31] Mitsutaka Fujita, Katsunori Wakabayashi, Kyoko Nakada, and Koichi Kusakabe. Peculiar localized state at zigzag graphite edge. *Journal of the Physical Society of Japan*, 65(7):1920–1923, 1996.

[32] Mitsuhiro Arikawa, Yasuhiro Hatsugai, and Hideo Aoki. Edge states in graphene in magnetic fields: A specialty of the edge mode embedded in the n=0 landau band. *Phys. Rev. B*, 78:205401, Nov 2008.

[33] V. P. Gusynin, V. A. Miransky, S. G. Sharapov, I. A. Shovkovy, and C. M. Wyenberg. Edge states on graphene ribbons in magnetic field: Interplay between dirac and ferromagnetic-like gaps. *Phys. Rev. B*, 79:115431, Mar 2009.

[34] M. Abramowitz and I.A. (Eds.) Stegun. *Handbook of Mathematical Functions with Formulas, Graphs, and Mathematical Tables.* New York: Dover, 1970.

[35] E.T. Whittaker. On the functions associated with the parabolic cylinder in harmonic analysis. *Proc. London Math. Soc.*, 35:417–427, 1902.

[36] E. Cojocaru. Parabolic cylinder functions implemented in matlab. *arXiv:0901.2220, Mathworks online database*, January 2009. URL: `http://www.mathworks.se/matlabcentral/fileexchange/22620`.

[37] Z. Jiang, E. A. Henriksen, L. C. Tung, Y.-J. Wang, M. E. Schwartz, M. Y. Han, P. Kim, and H. L. Stormer. Infrared spectroscopy of landau levels of graphene. *Phys. Rev. Lett.*, 98:197403, May 2007.

[38] P. Dean. The constrained quantum mechanical harmonic oscillator. *Mathematical Proceedings of the Cambridge Philosophical Society*, 62:277–286, 1966.

[39] Kristen Kaasbjerg, Kristian S. Thygesen, and Karsten W. Jacobsen. Unraveling the acoustic electron-phonon interaction in graphene. *Phys. Rev. B*, 85:165440, Apr 2012.

[40] Eduardo V. Castro, H. Ochoa, M. I. Katsnelson, R. V. Gorbachev, D. C. Elias, K. S. Novoselov, A. K. Geim, and F. Guinea. Limits on charge carrier mobility in suspended graphene due to flexural phonons. *Phys. Rev. Lett.*, 105:266601, Dec 2010.

[41] I. Arias and J. D. Achenbach. Rayleigh wave correction for the bem analysis of two-dimensional elastodynamic problems in a half-space. *International Journal for Numerical Methods in Engineering*, 60(13):2131–2146, 2004.

[42] Henrik Bruus and Karsten Flensberg. *Many-Body Quantum Theory in Condensed Matter Physics.* Oxford University Press, Oxford, 2009.

[43] D V Anghel and T Khn. Quantization of the elastic modes in an isotropic plate. *Journal of Physics A: Mathematical and Theoretical*, 40(34):10429, 2007.

[44] F. Guinea, M. I. Katsnelson, and A. K. Geim. Energy gaps and a zero-field quantum hall effect in graphene by strain engineering. *Nat Phys*, 6:30, January 2010.

[45] J.J. Sakurai. *Modern Quantum Mechanics*. Addison Wesley, revised edition, 1993.

[46] A. Vikström. Propagation of acoustic edge waves in graphene under quantum hall effect. *Low Temp. Phys.*, 41:381–388, Apr 2015.

[47] Weiwei Liu, Younho Cho, Haidang Phan, and JanD. Achenbach. Study on the scattering of 2-d rayleigh waves by a cavity based on bem simulation. *Journal of Mechanical Science and Technology*, 25(3):797–802, 2011.

[48] Alexander V. Savin and Yuri S. Kivshar. Vibrational tamm states at the edges of graphene nanoribbons. *Phys. Rev. B*, 81:165418, Apr 2010.

[49] Henry Wohltjen and Raymond Dessy. Surface acoustic wave probe for chemical analysis. i. introduction and instrument description. *Analytical Chemistry*, 51(9), August 1979.

[50] Sukru U. Senveli and Onur Tigli. A novel surface acoustic wave sensor for microparticle sensing and quantification. *IEEE Sensors Journnal*, 15(10), October 2015.

[51] Jiansheng Liu. A simple and accurate model for love wave based sensors: Dispersion equation and mass sensitivity. *AIP Advances*, 4:077102, 2014.

[52] G. McHale, M. I. Newton, and F. Martin. Theoretical mass sensitivity of love wave and layer guided acoustic plate mode sensors. *Journal of Applied Physics*, 91:9701, 2002.

[53] A. E. Borovik, E. N. Bratus, and V. S. Shumeiko. Hypersonic solitons in metals. *Sov. Phys. JETP*, 68:826–832, April 1989.